THE ASTROPHYSICAL JOURNAL, 324:869–892, 1988 January 15

SPATIAL AND SPECTRAL INTERPRETATION OF A BRIGHT FILAMENT IN THE CYGNUS LOOP

J. C. RAYMOND[1,2]
Harvard-Smithsonian Center for Astrophysics
J. J. HESTER[1,2]
California Institute of Technology
D. COX[1]
University of Wisconsin
W. P. BLAIR[1]
The Johns Hopkins University
R. A. FESEN[1]
University of Colorado
AND
T. R. GULL[1]
Goddard Space Flight Center
Received 1987 January 21; accepted 1987 July 8

ABSTRACT

Line profiles and surface-brightness maps of a bright optical filament in the Cygnus Loop show the filament to be a tangency of our line of sight to a surface bounded by a radiative shock wave. The thickness of the cooling and recombination zones behind the shock are at the limit of optical resolution so that the surface can be thought of as a thin emitting sheet. Optical and ultraviolet spectra, combined with detailed models, show that the shock velocity increases from ~ 80 km s^{-1} near its northwest end to 140 km s^{-1} at the southeast tip. The cooling and recombination behind the shock are complete ("steady flow") at its northwest end, but drastically incomplete in the southeast. We discuss the overall geometry which gives rise to the observed feature and the implications of the observations for resonance line scattering in the filament, elemental abundances, and grain destruction in the shock. The high quality and broad wavelength coverage of the data provide very strong tests of the shock models. It is quite satisfying that these spectra are in fact reproducible within a quite reasonable parameter space. By combining line profile information and absolute surface brightness with the shock velocity determined from the ultraviolet spectrum, we determine the preshock density and shock ram pressure. Comparison with the density obtained from the [S II] line ratio determines the nonthermal pressure (magnetic pressure plus cosmic-ray pressure) in the recombination zone, and we find that nonthermal pressure dominates.

Subject headings: nebulae: individual (Cygnus Loop) — nebulae: supernova remnants — shock waves — ultraviolet: spectra

I. INTRODUCTION

The filamentary optical appearance of old supernova remnants (SNRs) is so pervasive a feature that it is sometimes used to help distinguish SNRs from other nebulae. In the Cygnus Loop, the filaments are typically a few arcminutes in length (1′ is 6×10^{17} cm at 770 pc), 1″–5″ in width ($1–5 \times 10^{16}$ cm), and are arranged roughly parallel to each other over a scale of several parsecs. Figure 1 (Plates 27 and 28) shows Hα and [O III] images of the eastern limb of the Cygnus Loop (Hester, Parker, and Dufour 1983, hereafter HPD). Interpretations of the filaments have included ropes of emitting gas (e.g., Kirshner and Arnold 1979; Straka *et al.* 1986), intersecting shock waves (Bychkov and Pikel'ner 1975), or sheets of gas seen edge-on (Parker 1967; Miller 1974; Raymond *et al.* 1980). Among the hypotheses to account for edge-on sheets of emitting gas are shocks in individual clouds whose diameters equal the filament lengths (e.g., Raymond 1979), thermally unstable cooling of shocked gas (McCray, Stein, and Kafatos 1975; Smith and Dickel 1983), or tangencies of the line of sight with a much larger, slightly wavy sheet of emitting gas (Poveda and Woltjer 1968). The last interpretation has recently gained support from observations that bright filaments often bound regions of fainter diffuse emission and that the emission between filaments is spectrally identical to that of the filaments themselves (HPD). In addition, the wavy sheet hypothesis provides a compelling explanation for the nonthermal velocities observed in SNR filaments (Hester 1987).

To investigate the nature of the filaments, the physical conditions in the shocks, and the interaction between the X-ray–producing blast wave and the slower shocks which produce bright optical emission, we have chosen a filament in the southeast region of the Cygnus Loop for detailed optical and ultraviolet study. This filament, which runs from southeast to northwest, somewhat to the right of the center in Figure 1, was

[1] Guest observer with the *International Ultraviolet Explorer* satellite, which is jointly operated by NASA, the Science Research Council of the UK, and the European Space Agency.

[2] Visiting Astronomer, Kitt Peak National Observatory, National Optical Astronomical Observatories, operated by the Association of Universities for Research in Astronomy, Inc., under contract with the National Science Foundation.

PLATE 27

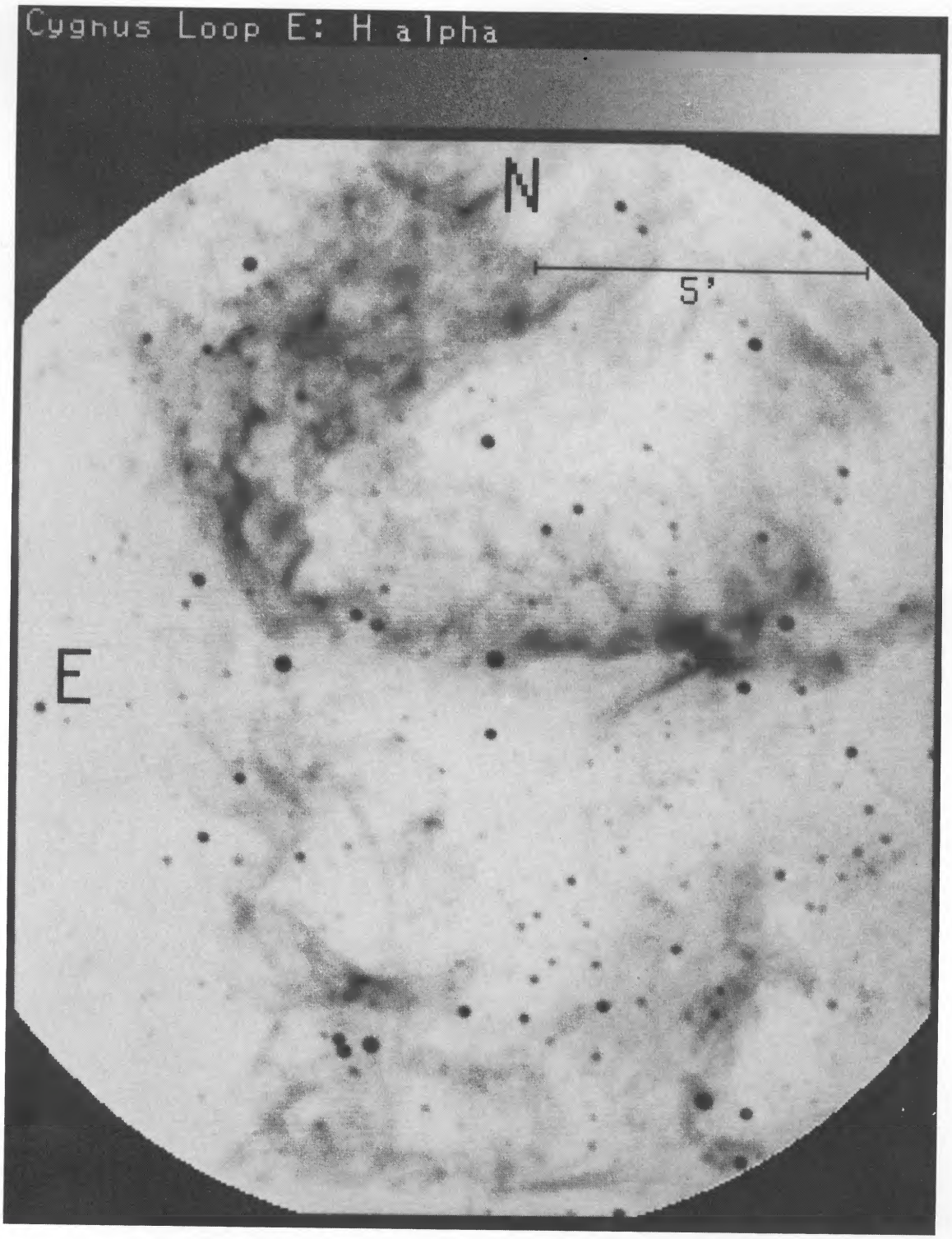

FIG. 1.—Images of SE region of Cygnus Loop in the [O III] λ5007 and Hα lines. Spur is 1.'5 feature ~2' west of star at center of field.

RAYMOND *et al.* (*see* **324**, 869)

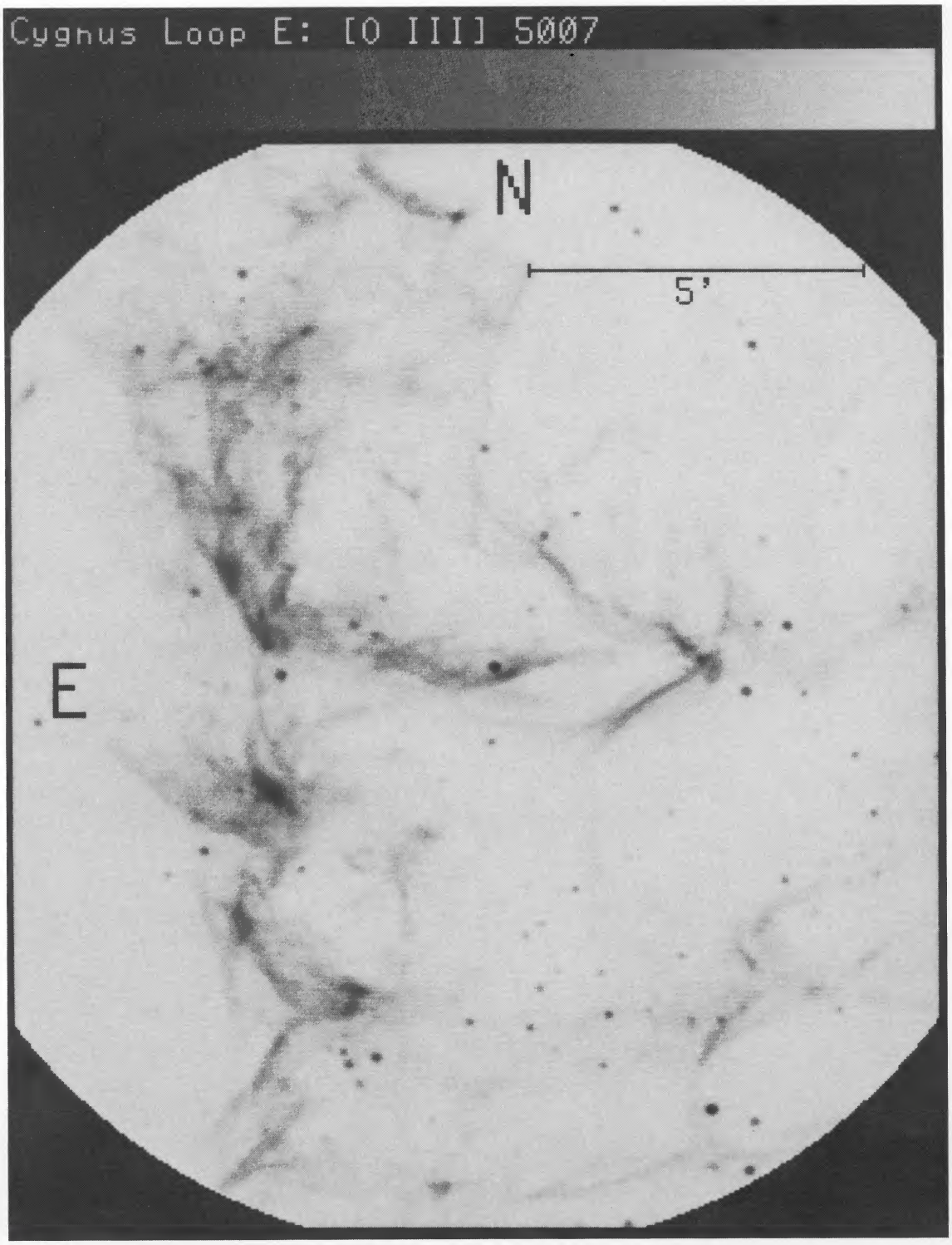

FIG. 1.—*Continued*

pointed out by HPD as being cleanly defined and much brighter than any foreground or background emission. The smooth progression of its [O III]/Hα ratio suggests a smooth change in shock velocity along its length. HPD refer to it as the spur.

Figure 2 (Plate 29) shows the spur region in greater detail, along with the positions of the apertures used for UV and optical observations. The spur is seen as an essentially straight, coherent structure, 1.'5 in length or $\sim 10^{18}$ cm at a Loop distance of 770 pc (Minkowski 1958). It is significantly interior to the projected edge of the Loop and runs obliquely to the local radius vector. At its northwest end it merges, at least in projection, with the very bright complex of Miller's (1974) position 2. At that end, its spectrum places it in HPD type I; that is, its modest [O III]/Hα ratio suggests a complete cooling region, with shock velocity somewhat below 100 km s^{-1}. The [O III]/Hα ratio increases smoothly toward the southeast end, however, placing the southeast reagion in HPD type II. Figure 3 (Plates 30 and 31) illustrates variation of these lines along the spur. HPD attributed the changing [O III]/Hα ratio to increasing shock velocity, but the increase is so severe that decreasing completeness of the recombination zone (nonsteady flow) is also required.

The spur thus presents students of SNR filaments with a remarkable laboratory. It has the appearance of a single uncomplicated structure. It is sufficiently bright for detailed study with existing instrumentation and sufficiently high in contrast for there to be little contamination by the surrounding diffuse emission (some of which is undoubtedly associated only in projection). It is a place where one can hope to model the UV and optical emission and at one end to check the models against optical spectra of a complete recombination region. By careful correlation of Doppler velocity data, surface brightnesses, and shock speed information obtained from the spectra, it is conceivable that one could construct a unique three-dimensional picture of the region, finding the shock surface geometry, line-of-sight depth, preshock density, and pressure. To that end we have obtained extensive UV and optical observations (§ II) and have constructed detailed numerical models of steady- and nonsteady-flow shock spectra and of the velocity and surface-brightness structures of wavy sheets (§ III). Results are presented in § IV.

II. OBSERVATIONS

Here we first describe the four sets of observations, then discuss the relative normalization and positioning of the different observations, and, finally, discuss the reddening corrections.

a) Surface Brightnesses of Optical Lines

HPD used a set of plates taken with narrow band filters to produce maps of the absolute surface brightnesses of the southeast section of the Cygnus Loop in the Hα, Hβ, [O I], [O II], [O III], and [S II] lines and in the 4400 Å continuum. Details of the reduction and accuracy of that data are given in HPD. For our purposes, the important characteristics of the data are the expected accuracy of the surface brightnesses in Hα and [O III] of 25%, the spatial resolution of ~3″, and the accuracy of the spatial positioning of 0.″3. Figures 1–3 belong to this data set.

b) Low-Resolution Optical Spectroscopy

Spectra were obtained at four positions along the spur in 1983 August using the Intensified Image Dissector Scanner (IIDS) on the 2.1 m telescope at Kitt Peak National Observatory with the 3.″8 × 12.″4 slit. These positions are shown in Figure 2. Low-dispersion spectra covering the wavelength range from 3600 to 7000 Å at 14 Å resolution and moderate-dispersion spectra covering the range from 6400 to 7700 Å at 7 Å resolution were obtained at each position. The observation times are given in Table 1. The spectra were reduced using standard KPNO IIDS reduction software. Standard KPNO atmospheric extinction values were used. Flux calibrations were based on BD +28–4211 and Feige 15. Line strengths were measured using the spectral reduction facilities at Rice University. The lower resolution spectra are shown in Figure 4.

TABLE 1

IIDS OBSERVATIONS

Position	Total On-Object Exposure	
	Low Dispersion (s)	Moderate Dispersion Red (s)
NW_a	1300	600
NW_b	1400	600
M	1200	600
SE	1200	600

Spectra from the two positions at the northwest end of the spur were summed on a pixel by pixel basis to yield a composite spectrum for comparison with the northwest *IUE* pointing discussed below. The moderate-dispersion red spectra were normalized to the low-dispersion spectra using the combined Hα plus [N II] line strengths, which could be measured accurately for each. Hα, [N II], and [S II] line strengths were then taken from the red spectra, in which all lines were well resolved. The measured line strengths are given in Table 2. The red

TABLE 2

OBSERVED OPTICAL FLUXES

Line	NW_a	NW_b	NW_{comb}	M	SE
[O II] λ3727	1476	1313	1431	1746	1472
[Ne III] λ3869	77	87	86	153	189
Hε, [Ne III] λ3967	38	42	40	55	68
[S II] λ4071	15	12	11	11	20
Hδ λ4102	22	21	20	18	23
Hγ λ4340	44	45	45	40	47
[O III] λ4363	22	36	27	57	92
[Fe III] λ4658	<2	<5	4	...	...
He II λ4686	<5	<12	8	...	...
[Fe III] λ4701	...	<3	2	...	...
Hβ λ4861	100	100	100	100	100
[O III] λ4959	128	189	153	395	424
[O III] λ5007	390	661	475	1277	1352
[Fe II] λ5159	<1	<2	3	...	...
[N I] λ5200	<4	<5	4	...	...
[Fe II, III] λ5266	<1	<1	<2	...	...
[N II] λ5755	8	12	9	9	...
He I λ5876	11	9	10	5	...
[O I] λ6300	36	42	40	32	38
[O I] λ6363	11	12	12	11	18
[N II] λ6548	117	126	125	130	124
Hα λ6563	399	412	405	379	328
[N II] λ6584	369	412	398	388	340
[S II] λ6717	...	...	153	110	139
[S II] λ6731	...	...	105	79	94
[Ar III] λ7136	...	...	23	55	42
[O II] λ7319	...	...	29	67	49
[O II] λ7330	...	...	20	24	20
F(Hβ)[a]	2.66	1.72	2.17	1.10	1.11

[a] Hβ flux in units of 10^{-14} ergs cm^{-2} s^{-1} in a 47 arcsec^2 aperture.

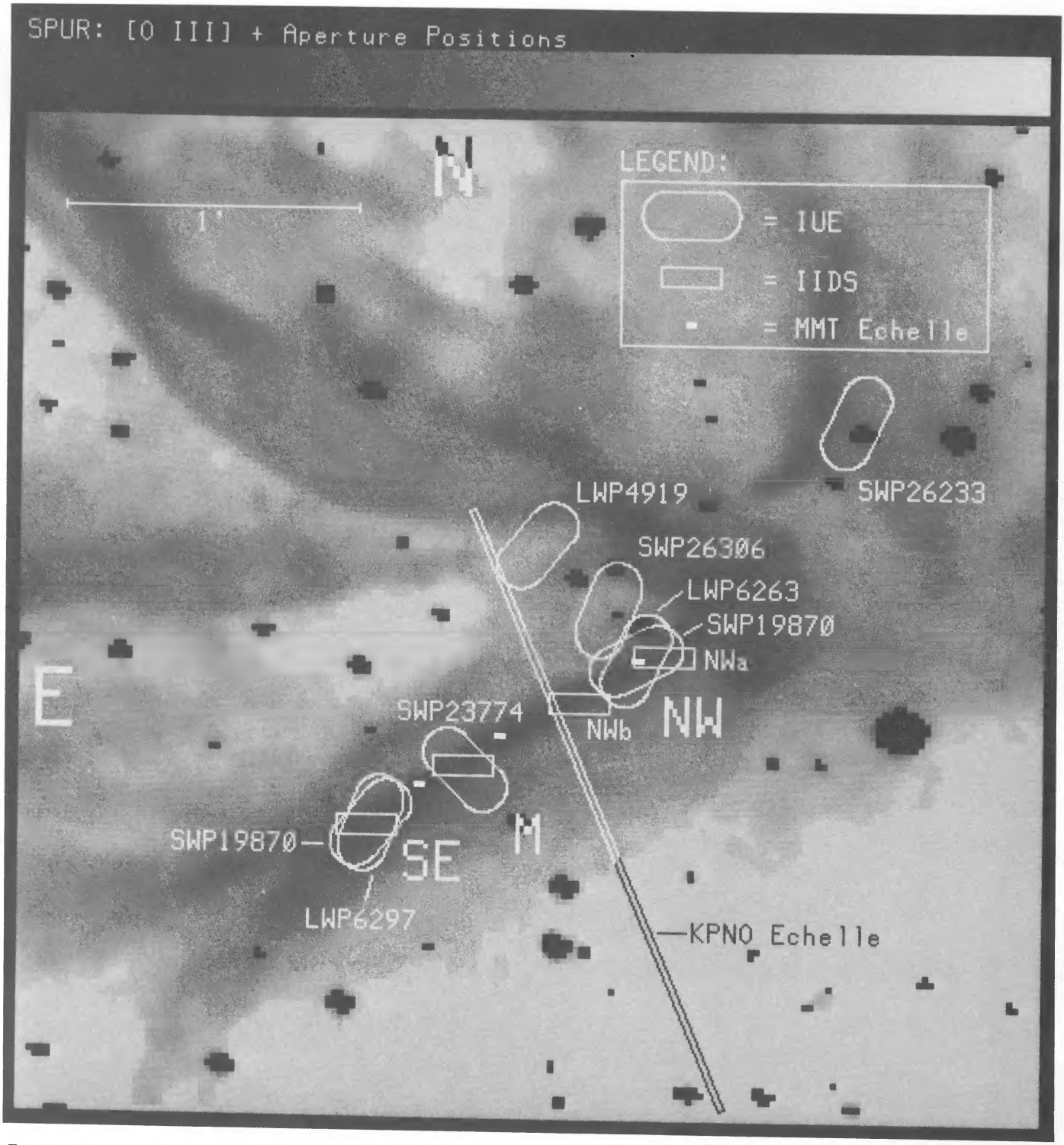

FIG. 2.—Spur in [O III] λ5007 showing aperture placements of *IUE* short-wavelength spectra, IIDS optical spectra, and MMT and KPNO echelle observations.

RAYMOND *et al.* (*see* **324**, 870)

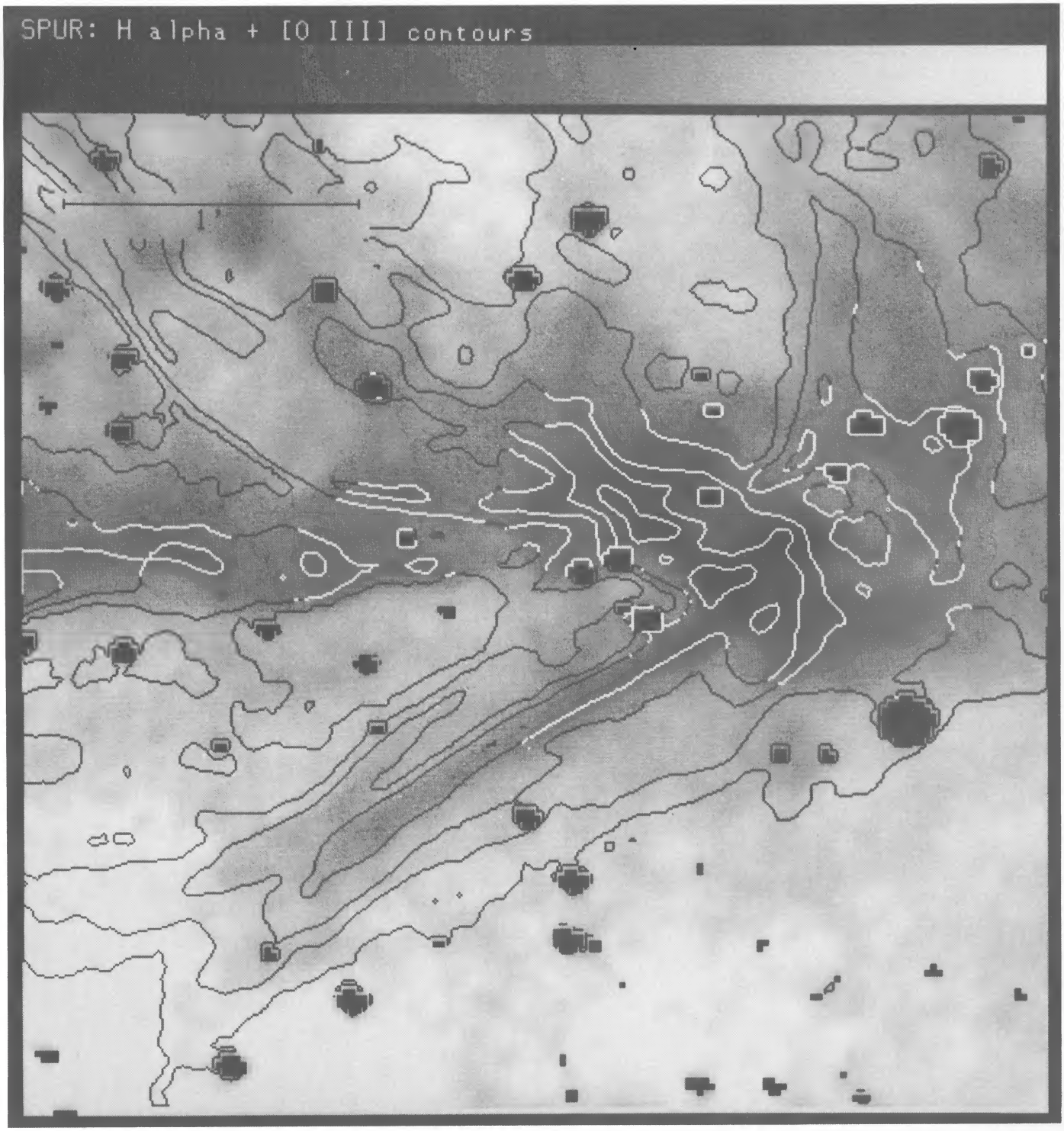

FIG. 3a

FIG. 3.—(*a*) Spur region [O III] intensity contours superposed on the Hα image. (*b*) Spur region Hα intensity contours superposed on the [O III] image.

PLATE 31

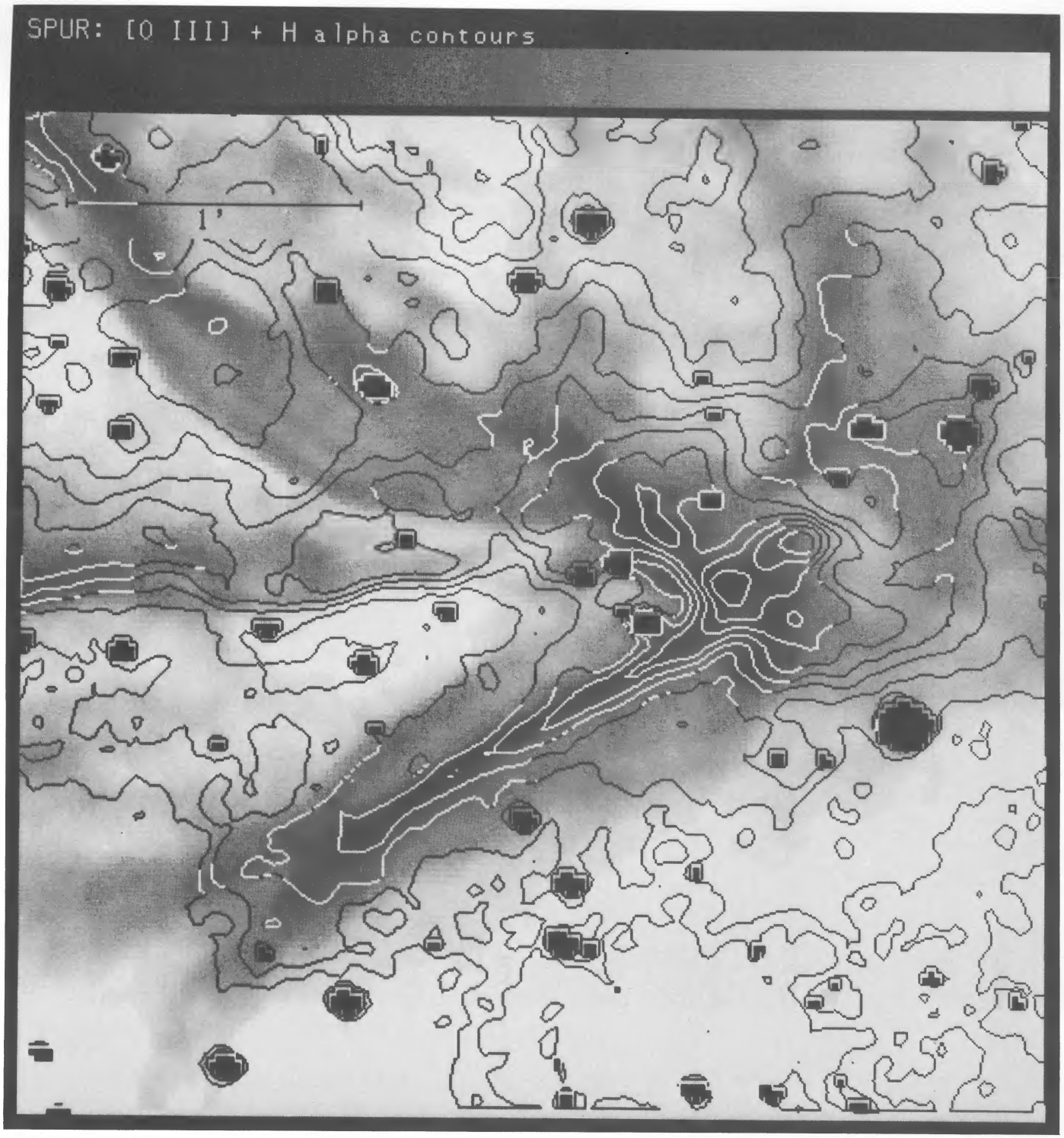

FIG. 3*b*

RAYMOND *et al.* (*see* **324**, 870)

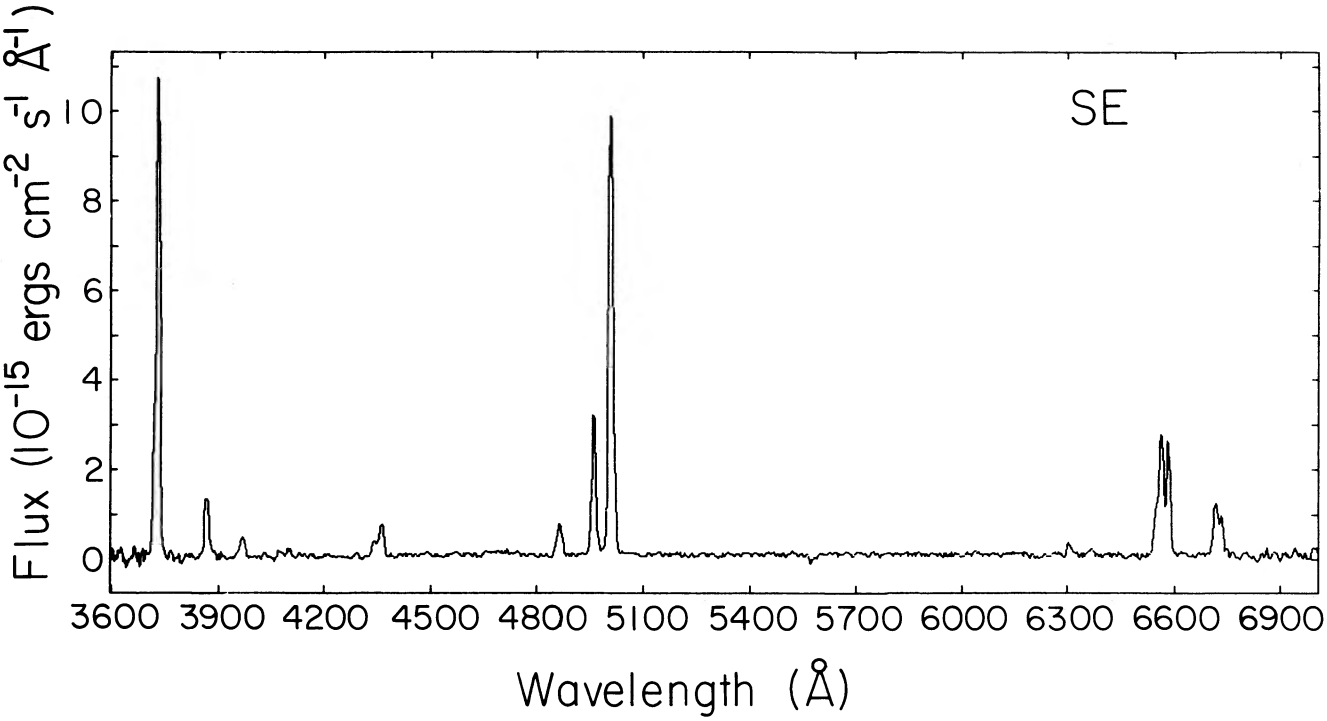

FIG. 4*a*

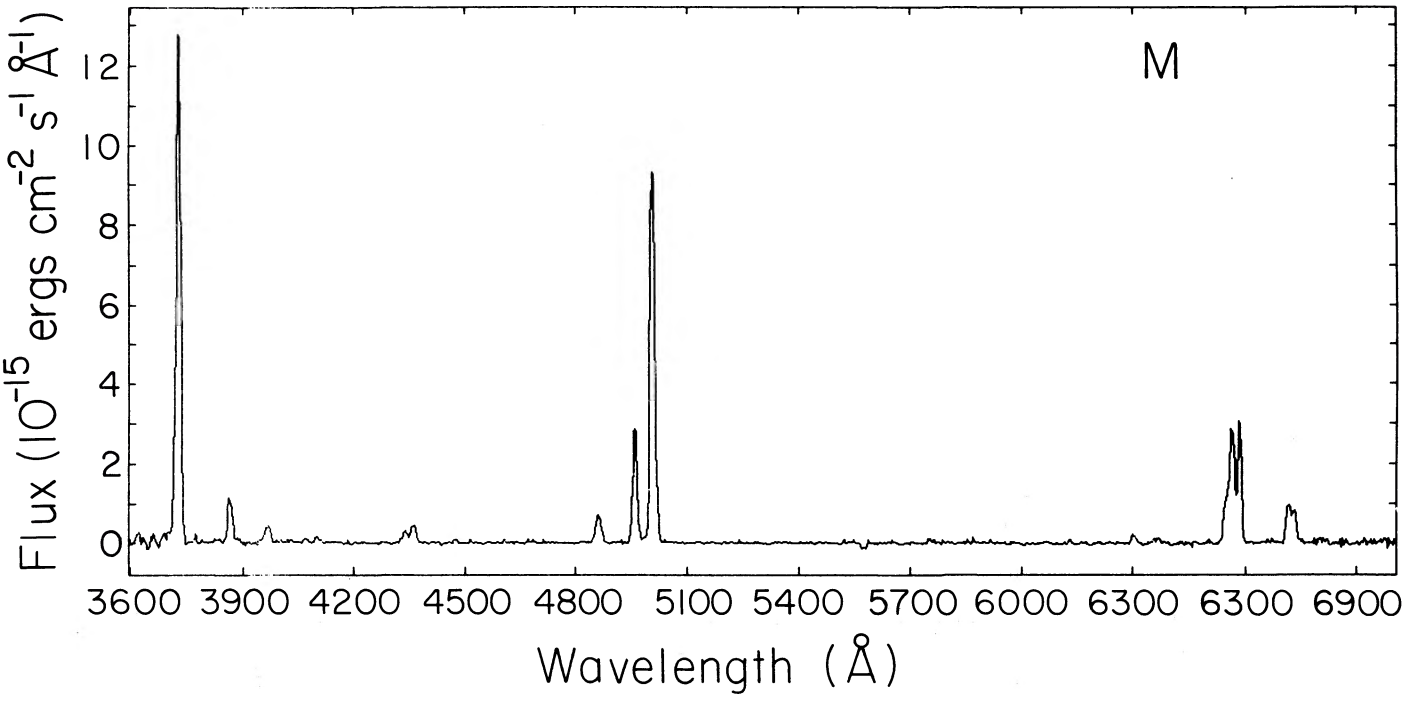

FIG. 4*b*

FIG. 4.—(*a*) Low-dispersion IIDS spectrum of position SE. (*b*) Low-dispersion IIDS spectrum of position M. (*c*) Low-dispersion IIDS spectrum of position NW_b. (*d*) Low-dispersion IIDS spectrum of position NW_a.

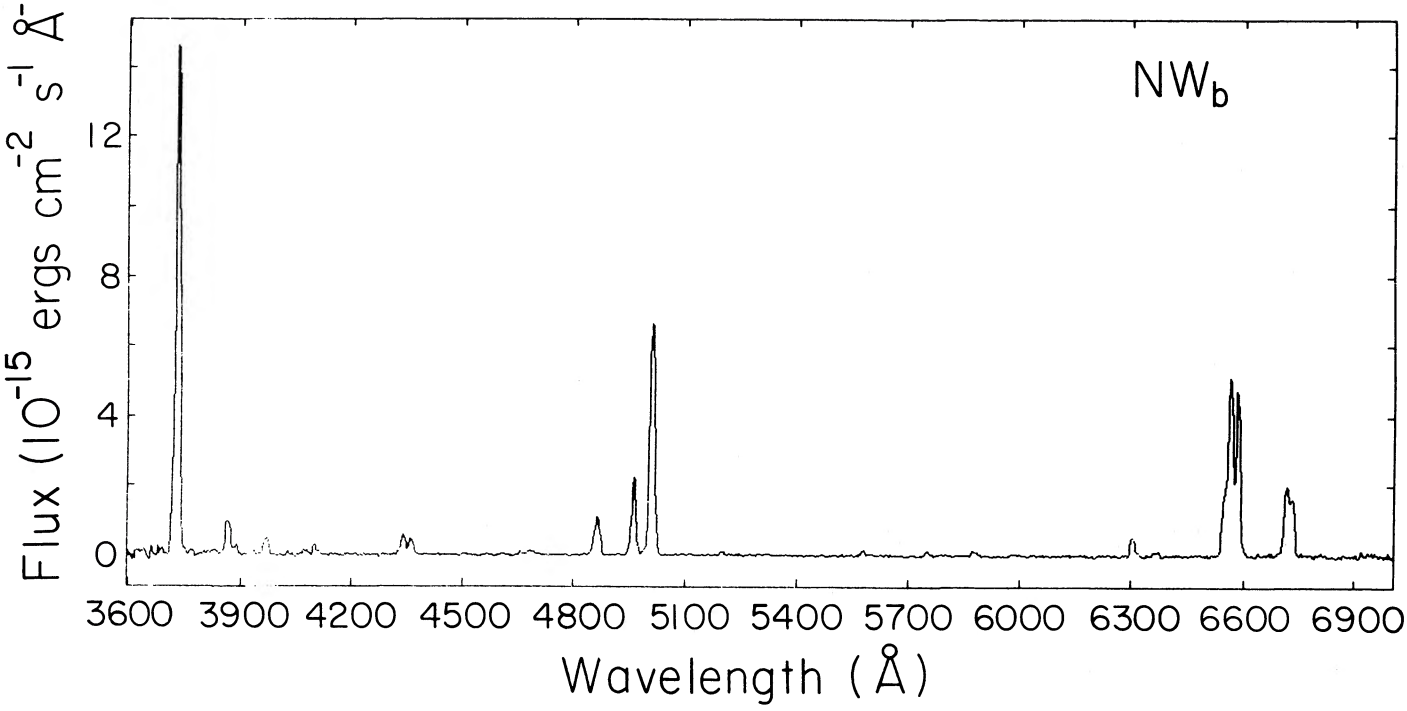

FIG. 4*c*

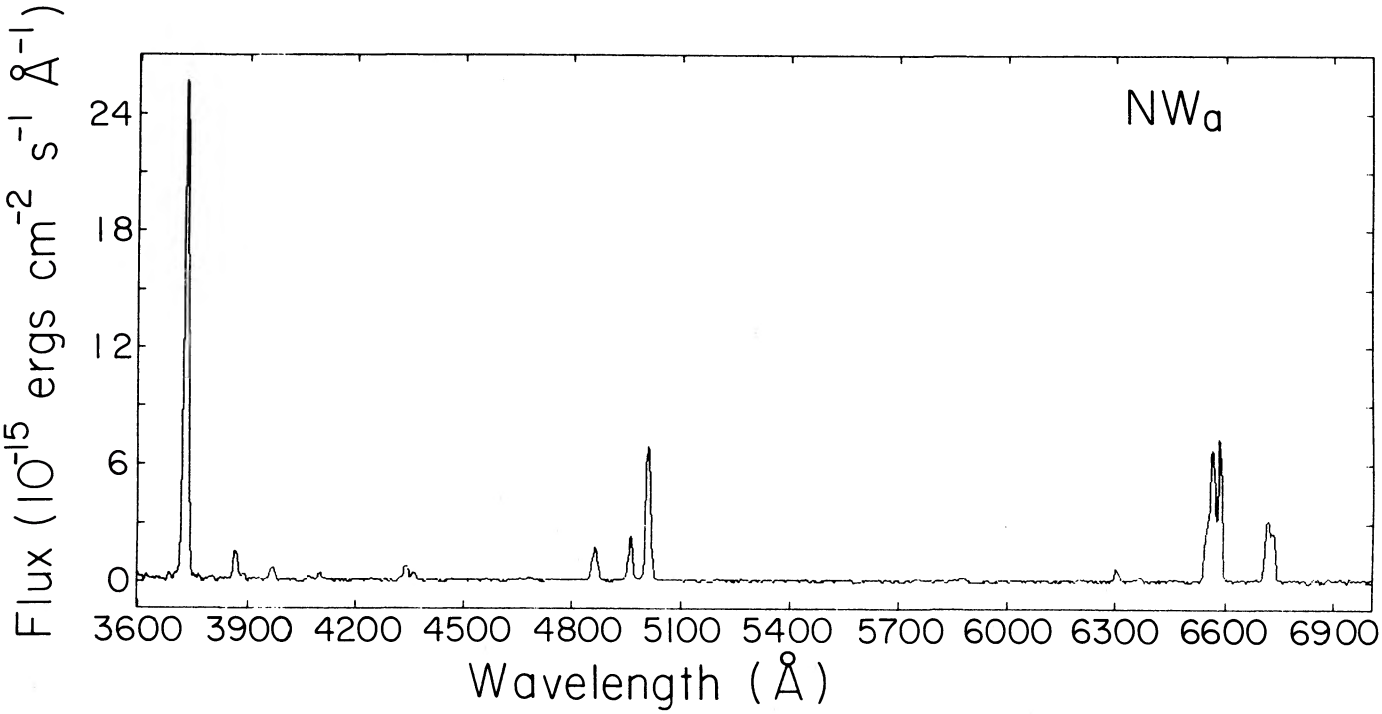

FIG. 4*d*

spectra at positions NW_a and NW_b were not reduced separately.

The uncertainties in the reported line strengths should be $\sim 15\%$ for the stronger lines and $\sim 50\%$ for the weakest lines. The absolute calibration of the Hβ flux is uncertain by at least 25% due to poor weather conditions during the observing run, and we will not rely on the absolute calibration in the analysis. There is an apparent systematic variation in Hα/Hβ of 20% in the spectra. However, J. J. H. has subsequently obtained narrow-band images in Hα and Hβ with a CCD detector at the 1.5 m telescope at Palomar Observatory, and the intensity ratio measured from these images shows that Hα/Hβ is constant to $\sim 5\%$ for the three positions. The discrepancy is probably due to a slight change in the calibration of the IIDS spectra near Hα over the course of the night. The spectrum which best matches the expected value of ~ 3 was bracketed by calibration observations. Other line ratios (e.g., Hγ/Hβ and [O II] $\lambda\lambda$7319, 7330/[O II] λ3727) do not show the systematic variation.

c) *High-Resolution Optical Spectroscopy*

Hα and [N II] line profiles were obtained at three positions along the spur using the echelle spectrograph on the MMT at the Fred L. Whipple Observatory in 1983 November. Profiles of the [O III] λ5007 line were obtained at the same three positions and at positions north and south of the middle spur position. The aperture positions are shown in Figure 2. A Reticon detector was used, and the wavelength scale was determined by comparison with a thorium-argon lamp. The $1'' \times 2''$ slit gave spectral resolution of 10 km s^{-1}. Figure 5 shows the [O III] profiles at the northwest (NW), middle (M), and southeast (SE) positions. They are quite similar to profiles reported by Shull *et al.* (1982), who observed the spur and other bright features in this section of the Cygnus Loop. We have fitted each of the profiles with two Gaussians (although the line asymmetries cast doubt on the usefulness of Gaussians to represent the data) in order to provide some measure of the line widths. All of the profiles require a component 30–40 km s^{-1} wide. We interpret this as part of the shock motion projected onto the line of sight (see Hester 1987). At each position, there is a second Gaussian component, and it is wider in Hα than in [N II]. Following Shull *et al.* (1982), we assume that these lines are formed at the same temperature and decompose the line widths into thermal and nonthermal components. This procedure yields temperatures of 10,800, 12,800, and 13,700 K and nonthermal velocities (FWHM) of 15, 11, and 15 km s^{-1} for positions NW, M, and SE, respectively. These values are quite similar to the values reported by Shull *et al.* for filaments in this section of the Cygnus Loop. The nonthermal velocities are analyzed in detail below.

Further high-resolution observations were obtained in 1985 September with the 4.0 m telescope at Kitt Peak. The echelle spectrograph was used with the TI-2 CCD and a 200 μm slit. We replaced the cross disperser with an optical flat and used narrow-band filters to isolate the [O III] and Hα plus [N II] orders in order to use the full 132″ length of the slit. The spectral resolution was 12 km s^{-1}, and the spatial resolution was limited by the seeing to 2″–3″. The slit was placed perpendicular to the spur, crossing it between positions M and NW (Fig. 2). The image was flat-fielded and corrected for distortions using IRAF softwar at Kitt Peak. The final images, placed on a velocity scale, are presented in Figure 6 (Plates 32 and 33).

d) *Ultraviolet Spectroscopy*

Ultraviolet spectra were obtained with the *IUE* satellite (Boggess *et al.* 1978). All fluxes pertain to the Large Aperture, a $10'' \times 20''$ ellipse covering 200 arcsec^2 (Panek 1982), whose orientation is determined by the spacecraft roll angle (Schiffer 1980). All blind offsets used BD +30–4248, the 10th magnitude star at the center of Figure 1. Offsets were less than 3′, so the positional accuracy is good to $\sim 1''$. Positions, position angles, and exposure times are listed in Table 3. For two of the short-wavelength (SWP) exposures, the long dimension of the *IUE* Large Aperture was placed along the filament to maximize the signal. At the middle position we placed the Large Aperture perpendicular to the spur to study spectral changes across the filament. Long-wavelength (LWP) exposures were obtained at the NW and SE positions. Aperture placements and orientations for the short-wavelength exposures are shown in Figure 2.

To make use of the spatial resolution along the *IUE* Large Aperture we have used the line-by-line files of the Guest Observer tapes to construct separate spectra for the left, middle, and right sections of the aperture, for a spatial resolution of $\sim 6''$. Particle events and known hot pixels (e.g., those near 1750 Å which affect the N III] line) were removed before the spectra were constructed. The SWP data were calibrated according to Bohlin *et al.* (1980), and the LWP spectra used the Cassatella

TABLE 3

IUE OBSERVATIONS

Image	Position	Exposure (minutes)	α, δ (1950)	Position Angle
		Spur Exposures		
SWP 19870.....	NW	360	$20^h54^m47^s.93$, +30°55′40″	−207°
SWP 23774.....	M	400	20 54 50.60, +30 55 27	+45
SWP 24612.....	SE	431	20 54 52.10, +20 55 16	−50
LWP 6263.....	NW	300	20 54 47.93, +30 55 50	−244
LWP 6297.....	SE	295	20 54 52.10, +30 55 16	−250
		Serendipitous Exposures		
SWP 26233.....	...	260	20 54 44.50, +30 56 39	−244
SWP 26306.....	...	290	20 54 48.35, +30 56 00	−250
LWP 4919.....	...	300[a]	20 54 49.50, +30 56 13	−50

[a] Total exposure time was 370 minutes, but during the first 70 minutes the camera was in high-dispersion mode. No trace of a high-dispersion signal is visible on the Photowrite image.

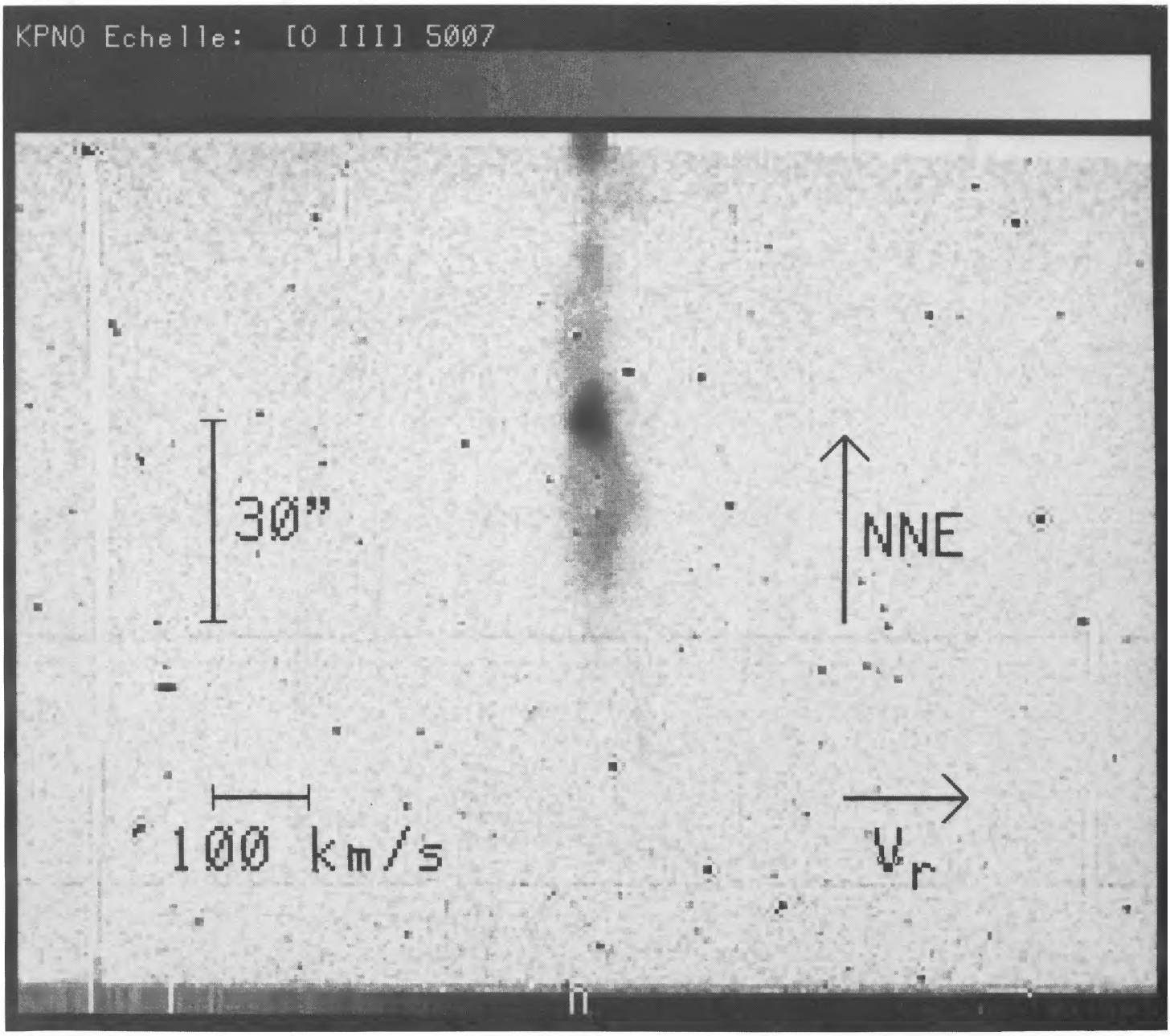

FIG. 6a

FIG. 6.—(*a*) Long-slit echelle observation in the λ5007 line. (*b*) Long-slit echelles observation of the Hα and [N II] λ6584 lines.

RAYMOND *et al.* (*see* **324**, 873)

PLATE 33

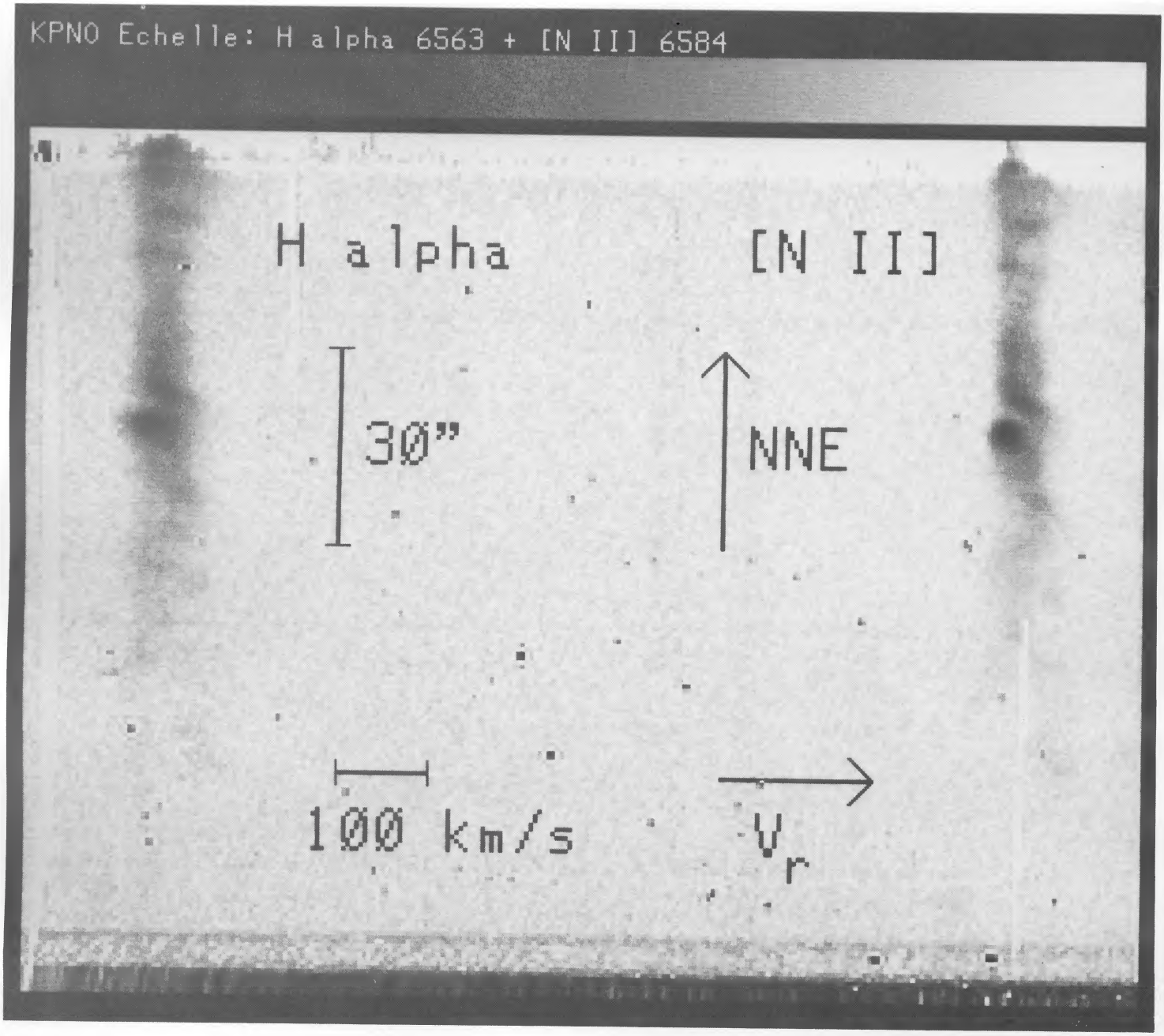

FIG. 6*b*

RAYMOND *et al.* (*see* **324**, 873)

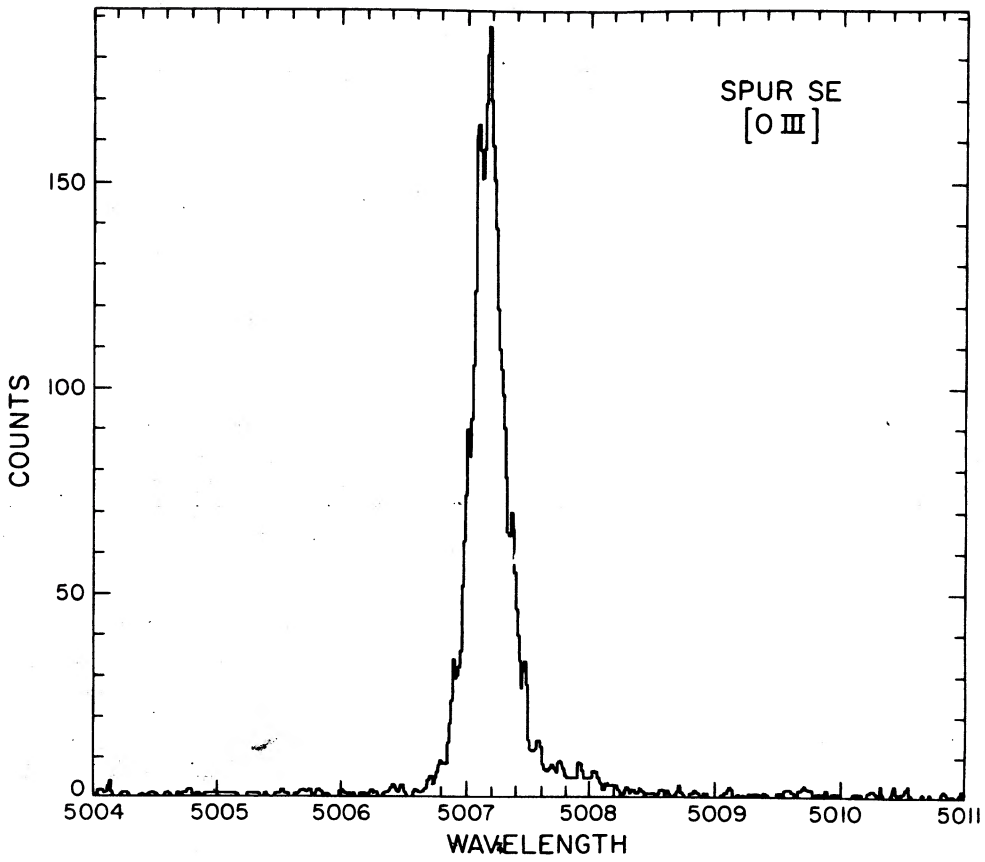

FIG. 5a

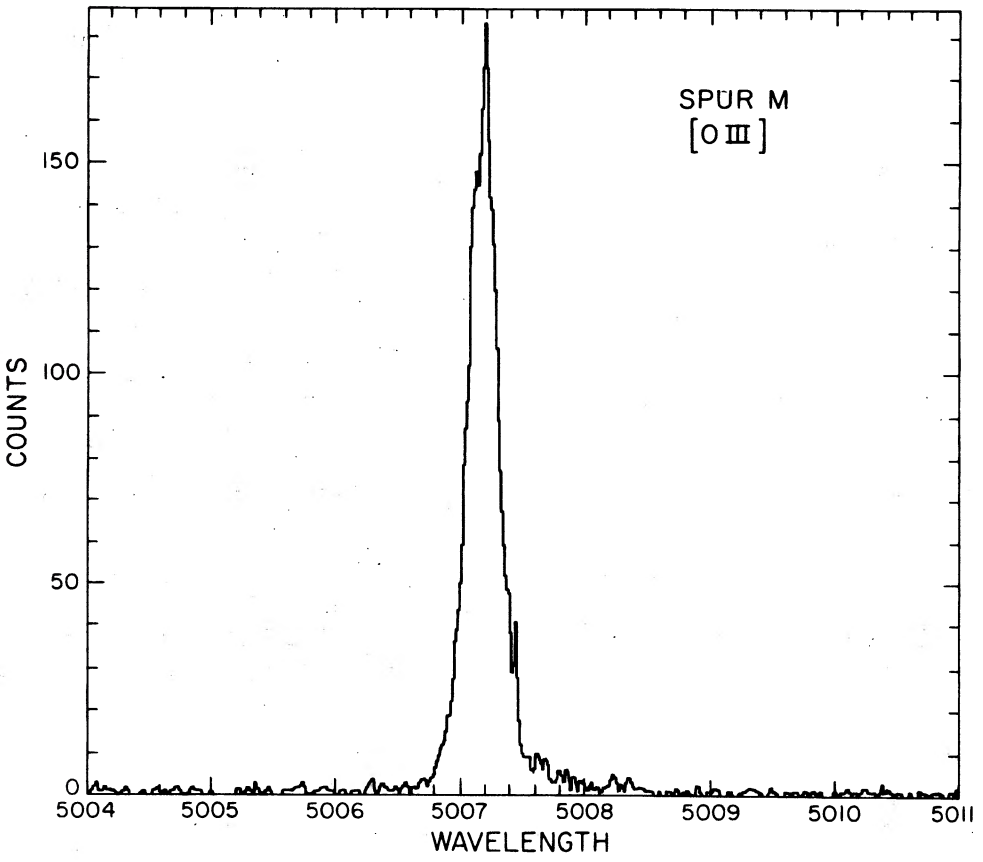

FIG. 5b

FIG. 5.—(*a*) MMT echelle [O III] λ5007 line profile of positions SE. (*b*) MMT echelle [O III] λ5007 line profile of positione M. (*c*) MMT echelle [O III] λ5007 line profile of position NW.

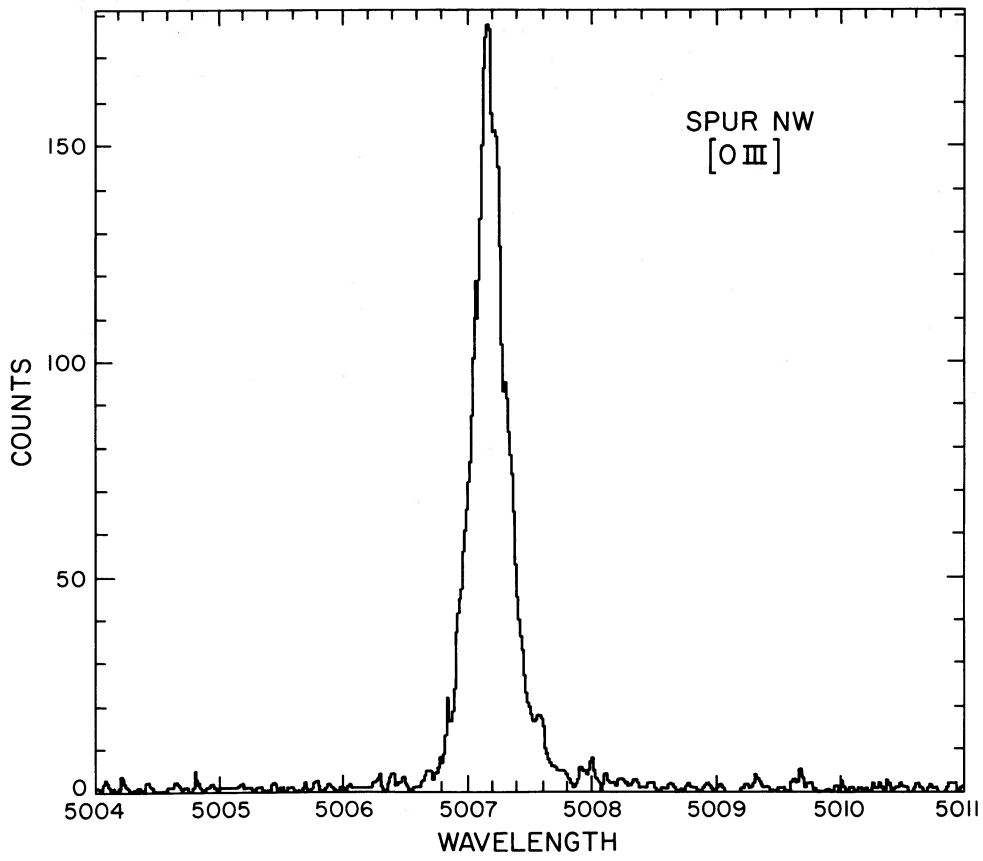

FIG. 5c

and Harris (1983) calibration. As the signal in the spectra of the separate sections is quite poor in the weaker lines, we present in Table 4 and Figure 7 only the fluxes from the entire Large Aperture. The variations of the strongest lines across the aperture will be discussed in the context of the interpretation.

During each short- or long-wavelength exposure on the spur, the *IUE* camera for the other wavelength range was simultaneously exposed, giving a serendipitous spectrum of a position 66″ from the target position. The position angle of this 66″ displacement was determined from the spacecraft roll angle (Shiffer 1980). Three of these exposures fell upon Cygnus Loop nebulosity bright enough to produce usable spectra, and these exposures are included in Tables 3 and 4. SWP 26233 is 49″ north and 44″ west of the NW spur position, placing it on the upper edge of the bright nebulosity of Miller's (1974) position 2. This position is 26″ north and ~14″ west of the *IUE* observation of Benvenuti, Dopita, and D'Odorico (1981) listed as CL 2. The line and continuum fluxes of these two *IUE* exposures are similar, except that SWP 26233 shows stronger high-excitation (C IV and N V) emission and weaker low-excitation emission. SWP 26306 was located 10″ north and 5″ west of the NW spur position, so that it was not located on the bright ridge of the spur itself, but on the diffuse region which surrounds the spur. The surface brightness was so low that only the C III] and C IV lines could be measured with confidence. However, the low C IV:C III] ratio confirms that this diffuse emission is spectrally similar to that of the NW position. Finally, LWP 4919 is the spectrum of a region 23″ north and 20″ east of the NW spur position, and about half of the Large Aperture fell on the bright nebulosity of Miller's position 2. The strong C II] and the absence of [O II] λ2470 and [Ne IV] λ2420 show that this is a low-velocity shock, probably even slower than the shock at NW.

e) Normalization

Combining the optical and ultraviolet spectra enhances the usefulness of both. This is often difficult due to the differing aperture shapes and sizes used for observing at different wavelengths and to variations of surface brightness within the aperture used for a single observation. These problems could be especially severe for the *IUE* exposure at the central position, where only about half of the *IUE* Large Aperture showed bright emission, and for the NW position, where the rapid change in the [O III]/Hβ ratio suggests that the shock velocity varies along the 20″ length of the *IUE* aperture.

We projected the *IUE* aperture onto the HPD [O III] raster and summed the included surface brightness to obtain the optical [O III] absolute flux from the region observed by *IUE*. The fluxes of the other optical lines relative to [O III] were taken from the IIDS spectra, and the complete spectra were then renormalized to Hβ = 100 for convenience in comparison with model spectra. This procedure is accurate to the calibration uncertainties of *IUE* (~10%) and the HPD raster (25%). It deals with the problems of differing UV and optical apertures far more effectively than have previous analyses of UV and optical spectra. The HPD images show that the relative line strengths change rapidly at the northwest end of the spur. We obtained IIDS spectra at the ends of the *IUE* aperture and found that the shock velocity change was substantial. The spatially resolved *IUE* spectrum was broken down into

TABLE 4

ULTRAVIOLET EMISSION (10^{-13} ergs cm^{-2} s^{-1})

A.

Line	SWP 19870	SWP 23774	SWP 24612	SWP 26233	SWP 26306
N v λ1240	<0.22	0.57	1.20	1.21[a]	...
C II λ1335	0.20	0.15[a]	<0.33	...	...
O IV], Si IV λ1400	0.63	1.05	2.70	0.95	...
N IV] λ1484	0.29[a]	0.66	1.67	...	...
C IV λ1550	1.05	1.32	2.98	3.38	0.86
He II λ1640	0.69	0.39	1.34	0.69	...
O III] λ1666	2.10	2.40	3.74	1.51	...
N III] λ1750	1.15[a]	1.02[a]	1.65[a]	1.14[a]	...
Si III] λ1890	0.50	0.54	0.48	2.25	...
C III] λ1909	6.01	3.57	6.57	5.59	3.06
2γ	18.1	11.1	7.2	38.0	23.3

B.

Line	LWP 6263	LWP 6297	LWP 4919
C II] λ2325	4.50	1.16	6.36
[Ne IV] λ2420	...	0.27	...
[O III] λ2470	0.81[a]	0.31	...
Mg II λ2800	...	...	1.00

[a] Measured flux affected by particle event or hot pixel.

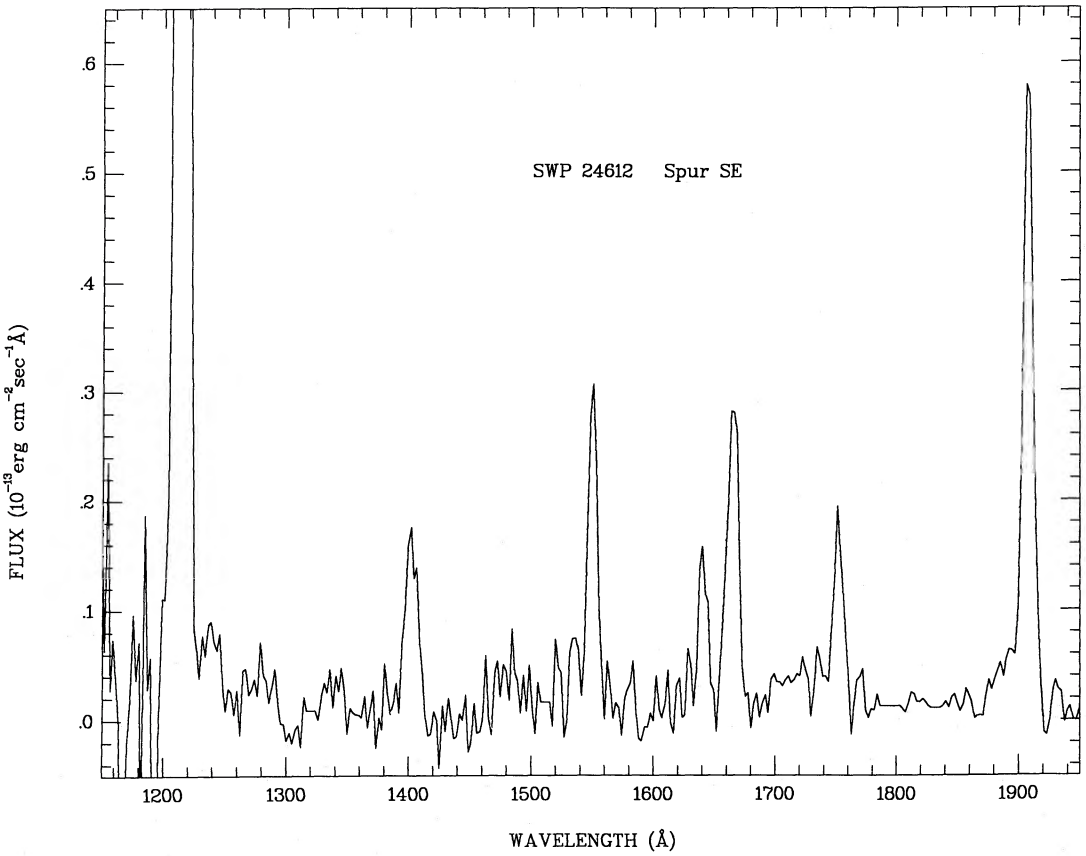

FIG. 7a

FIG. 7—(*a*) *IUE* short-wavelength spectrum of position SE. (*b*) *IUE* short-wavelength spectrum of position M. (*c*) *IUE* short-wavelength spectrum of position NW.

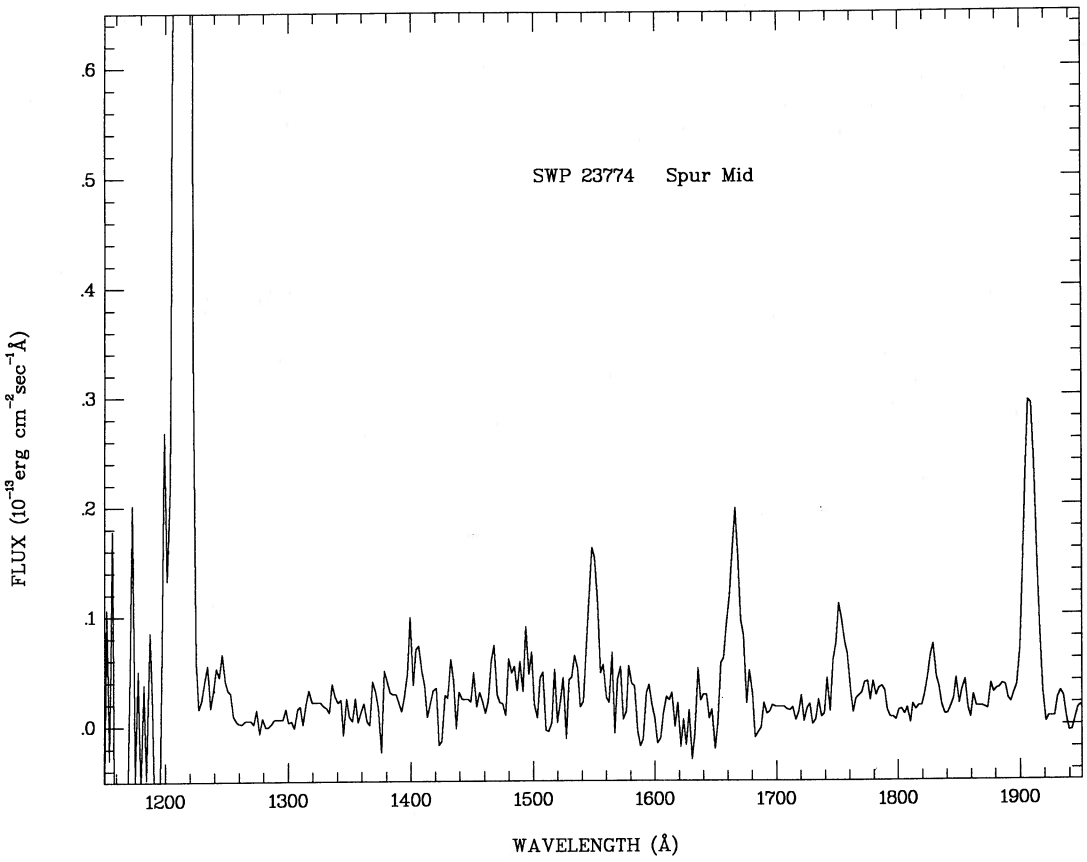

FIG. 7*b*

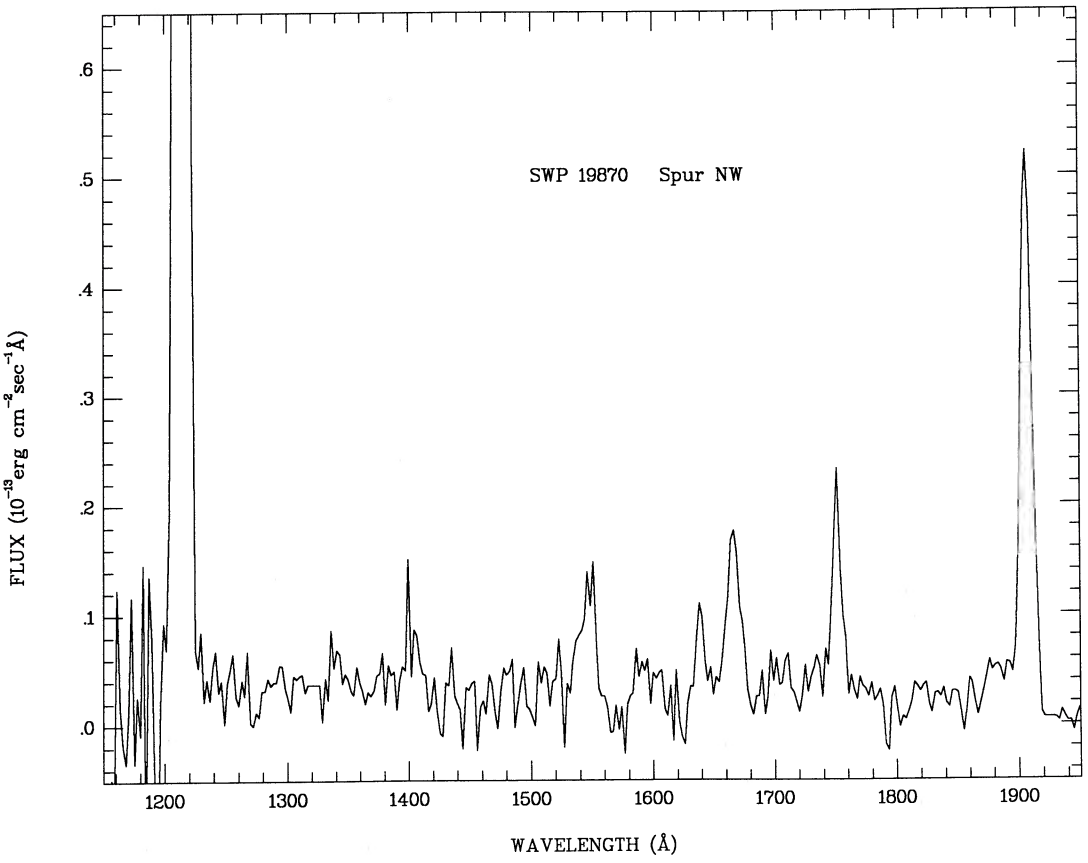

FIG. 7*c*

individual spectra from sections of the Large Aperture, but these individual spectra are too noisy to be of much use except in confirming that the UV emission is concentrated toward the southeast end of the Large Aperture. We therefore combined the UV spectrum with the average of the two IIDS spectra to obtain an average shock spectrum and use the individual IIDS spectra to estimate the actual velocity spread.

f) Reddening and Corrected Spectra

The usual reddening value taken for the Cygnus Loop is $E(B-V) = 0.08$ (Parker 1967; Raymond *et al.* 1981), though Benvenuti, Dopita, and D'Odorico (1980) assumed a color excess of zero in order to improve the agreement of the two-photon continuum flux with that expected from their models. The ratio of O III] λ1664 to [O III] λ5007 tends to support a reddening estimate of $E(B-V) = 0.08$ with Seaton's (1979) average reddening curve, however. We therefore make this reddening correction and use the UV-to-optical normalization procedure described above to obtain spectra for comparison with models. The fluxes relative to Hβ for the three spur positions are listed in Table 5. We do not have IIDS spectra for the serendipitous *IUE* positions, but fluxes for several lines were obtained from the HPD rasters, and reddening-corrected optical and UV spectra for the three serendipitous positions are listed in Table 6.

The absolute Hβ surface brightnesses are averages over the regions within the *IUE* Large Aperture. As noted earlier, the Hα fluxes at positions M and NW are 10%–20% too large relative to Hβ, and it is likely that lines at neighboring wavelengths are similarly overestimated. The ratios of UV lines to Hβ contain the 25% uncertainty in the optical surface brightness, the 10% *IUE* calibration uncertainty, and a $\sim$20% uncertainty in reddening correction, so we estimate the overall uncertainty to be about $\sim$35%. The two-photon continuum is badly underexposed in all the spectra, so we estimate a 50% uncertainty in its ratio to Hβ.

As a check on the overall accuracy of the flux normalization and reddening correction, we examine the ratio of the [O III] lines in the UV and optical. This ratio depends only weakly on the details of the shock models, since it depends only on the ratio of collision strengths of the lines and the Boltzmann factor corresponding to the difference in excitation potentials.

TABLE 5

OBSERVED AND PREDICTED FLUXES RELATIVE TO Hβ

	SE		M		NW	
LINE	Observed	Model	Observed	Model	Observed	Model
N v λ1240	261	418	109	48	<19	1
C II λ1335	68[a]	486	29[a]	717	16[a]	341
O IV] λ1400	537	675	182	401	55[b]	36
N IV] λ1486	131	222	123	129	22[b]	16
C IV λ1550	575[a]	6800	221[a]	4330	76[a]	399
He II λ1640	255	275[c]	65	166[c]	50	21[c]
O III] λ1664	712	537	359	427	150	142
N III] λ1750	323[b]	206	175[b]	167	85[b]	60
Si III] λ1890	98	185	180	261	38	214
C III]1909	1340	1420	640	1570	646	617
C II] λ2325	291	454	...	596	386	272
[Ne IV] λ2420	66	219	...	140	...	9
[O II] λ2470	69	43	...	44	68	27
[O II] λ3727	1601	1730	1650	1720	1280	893
[Ne III] λ3869	203	100	141	96	72	34
[S II] λ4071	21	19	10	21	28	11
[O III] λ4363	92	91	49	74	22	25
[Fe III] λ4658	...	19	...	24	4	12
Hβ λ4861	100	100	100	100	100	100
[O III] λ4959	421	433	339	353	125	109
[O III] λ5007	1388	1290	1090	1050	338	326
[N I] λ5199	...	9	...	12	4	12
[N II] λ5755	...	10	8	10	7	4
He I λ5876	...	9	5	10	7	17
[O I] λ6303	35	34	26	36	31	25
[O I] λ6363	17	11	5	12	9	8
[N II] λ6548	114	137	103	131	94	57
Hα λ6563	300	303	300	304	300	304
[N II] λ6584	311	410	307	393	298	171
[S II] λ6717	126	104	86	116	115	72
[S II] λ6731	85	77	62	86	78	53
[Ar III] λ7136	44	61	42	50	17	20
[O II] λ7319	44	32	52	32	29	20
[O II] λ7330	18	26	18	26	15	16
2-photon	1400	1420	1220	1550	1480	1400
F(Hβ)[d]	1.84	0.092	1.51	0.107	4.58	0.243

[a] Resonance line affected by scattering.

[b] Uncertain flux due to camera defect, particle, event, or weakness of line.

[c] Models assume case A for excitation and case B for recombination.

[d] Surface brightness in units of 10^{-5} ergs cm^{-2} s^{-1} sr^{-1}. Model surface brightnesses are for face-on shocks.

TABLE 6

INTENSITIES RELATIVE TO Hβ FOR SERENDIPITOUS POSITIONS

Line	SWP 26233	SWP 26306	LWP 4919
N v λ1240	110	...	...
O iv λ1400	79	...	...
C iv λ1550	275	70	...
He ii λ1640	55	...	...
O iii] λ1664	111	...	...
N iii] λ1750	91	...	...
Si iii] λ1890	185	...	...
C iii] λ1909	458	242	...
C ii] λ2325	...	...	529
Mg ii] λ2800	...	...	69
[O ii] λλ3627, 3729	712	754	967
Hβ	100	100	100
[O iii] λ5007	224	191	102
Hα	284	235	286
[N ii] λ6584	189	183	207
[S ii] λλ6717, 6725	360	201	509
2γ	3120	1920	...
F(Hβ)[a]	5.41	3.58	5.63

[a] 10^{-5} ergs cm^{-2} s^{-1} sr^{-1}.

The observed ratios agree with those predicted by the models to within the calibration uncertainties in all cases (Table 5).

III. MODELS

Evidence which we have discussed elsewhere at length (HPD; Hester 1987) strongly supports the view that the Cygnus Loop filaments and their neighboring diffuse emission arise from an extremely thin two-dimensional surface (a sheet). The sheet is in fact a shock wave in the interstellar medium, moving into sufficiently high-density material for the radiation from the post shock gas to be detectable, particularly in zones of near tangency to the line of sight. Irregularities in the sheet geometry lead to the complex filamentary appearance, such irregularities deriving naturally from slight density variations in the preshock density.

In some regimes, Balmer lines dominate the optical emission of the shock. These have been successfully modeled as fairly high velocity ($v_s > 150$ km s^{-1}) "nonradiative" shock waves, the Balmer emission arising from a narrow zone of postshock ionization of neutral hydrogen (Raymond *et al.* 1983; Fesen and Itoh 1985; Hester, Raymond, and Danielson 1986).

In other regimes, models of plane-parallel steady-flow radiative shockwaves have been used with some success. In such models, the shock is followed immediately by a thin region of rapid collisional ionization, then by a more extended cooling region in which the temperature drops from the postshock value (1.5×10^5 K for 100 km s^{-1}) to $\sim 10^4$ K, and then by a zone of photoionization and recombination which absorbs ionizing UV from the cooling region and radiates forbidden and recombination lines of low-ionization stages. The whole structure is approximately isobaric and high densities are reached as the temperature falls, finally being limited by the pressure of the magnetic field. The inferred velocities for filaments with spectra consistent with such models are, in general, 70–150 km s^{-1}, with inferred preshock densities somewhat higher than for the Balmer line filaments. This picture is consistent with the calculations of the cooling times required to establish a structure resembling a complete radiative shock front.

Intermediate cases, however, are clearly present, and, as mentioned in the introduction, the spur filament is one which shows both an apparent gradient in shock velocity (low in NW and high in SE) and a corresponding gradient in the completeness of the "recombination region" behind the shock. In its interpretation we therefore require models which address this incompleteness in the spectrum in a quantitative manner.

The transition from nonradiative to radiative shock fronts, and the structure of the latter, may be complex. But, when a shock front has been moving into material of given density for a time comparable to the cooling time scale in the postshock material, there begin to be regions in the postshock flow in which the temperature has decreased substantially due to its radiation history. Owing to the sensitivity of this time scale to preshock density and to the thermal instability of the postshock flow (McCray, Stein, and Kafatos 1975), one cannot expect a perfectly laminar temperature distribution. The trailing, cooler gas may be lumpy or stringy and, to some extent, embedded in the uncooled gas.

The cooling time scale, and hence the cooling region thickness, vary sensitively with shock speed for fast shocks. As a consequence, the formation of a steady radiative structure may be preceded by a period of fitful lurching of the shock velocity and the development of secondary shocks (Straka 1974; Falle 1975; Chevalier and Imamura 1982; Innes, Giddings, and Falle 1986; Bertschinger 1986).

This instability may have little to do with the filaments observed in remnants such as the Cygnus Loop. The velocity range of applicability quoted is higher than that inferred for the radiative shocks (above and below 150 km s^{-1}, respectively). Perhaps the instability depends on the boundary conditions assumed for the calculations or is present only in a one-dimensional world. Certainly, complexity in the observed filamentary structure does not require a corresponding complexity in the emission region: mild distortions in the geometry of the emitting surface are sufficient (Hester 1987).

On the other hand, simplicity may be a fond hope, reinforced by selection effects. In the spur, for example, we have chosen a filament which appears to be a prime candidate for description and analysis in simple terms. Although we have not identified any regions in the Cygnus Loop where shock lurching is an important attribute of the structure, such places may be present and could be common. Such complications might be relevant to the morphological differences between the crisp, arcuate [O iii] filaments and the more diffuse Hα emission patterns (Parker 1973; Fesen, Blair, and Kirshner 1982). In the case of the spur, we derive the ram pressure below and show that it is substantially larger than either the thermal pressure in the recombination region or that found in the X-ray–emitting gas. This could conceivably be an example of the sort of pressure variation one might expect from the instability.

Despite the possibility of these instabilities, we have found no evidence in our study of the spur that such complications are relevant to it. The feature is, in all respects, smooth in space, radial velocity structure, and spectral variation. In addition, we shall demonstrate that its line-of-sight depth is very great, certainly eliminating all possibility that it is a ropelike feature. (We, in fact, follow it off tangency to the line of sight in velocity and surface-brightness structures.) It must certainly be unlikely for a process as nonlinear as thermal instability to operate coherently over a surface as large as that represented by the spur, which it would have to do to account for the smooth distributions observed.

With this background in hand we now discuss the simple models required for the interpretation of the data we have

acquired on the spur. These models are of two types, one an attempt to represent the spectra of shock waves which, although steady, are so far, too young to have established a complete recombination zone. The other is a representation of the line-of-sight velocity distribution of a distorted sheet.

a) Spectral Models

Our approach to the representation of the spectra of radiative shocks with incomplete cooling regions is to model steady state shockwaves with completed structures, but to present running spectra, integrated from the shock. In short, we assume that the "recombination regions" which are too young to have accumulated enough material to be optically thick (to the UV from the cooling region) have similar temperature and density distributions to that portion of a complete cooling region with the same integrated column density.

To first order, this must be a reasonable approximation. The UV emission is not sensitive to the degree of completeness of the recombination zone. Some fraction of the UV is caught and fluoresced to optical and IR radiation by the colder material whether the colder material be accurately planar or fairly lumpy in distribution. To second order, however, details of radiative transfer, particularly of the "diffuse radiation" arising from hydrogen recombination to the ground state must be incorrect in this approximation. Fortunately, experience with shock modeling including only forward (downstream) radiative transfer shows that the effect is truly secondary.

A number of models have been constructed for the spectra of complete cooling regions (Cox 1972*a*; Dopita 1977; Raymond 1979; Shull and McKee 1979; Binnette, Dopita, and Tuohy 1985; Cox and Raymond 1985; Hartigan, Raymond, and Hartmann 1987). The reliability of the shock models can be assessed from the level of agreement among the different models discussed by Pequinot (1986). The integrated spectra include both the cooling region components and the forbidden and hydrogen line radiation of the recombination region. A few truncated models of incomplete shocks have previously been computed to match individual filaments, such as Miller's position 3 in the Cygnus Loop (Raymond *et al.* 1980; Contini and Shaviv 1982) and a low-excitation HH object (Dopita, Binnette, and Schwartz 1982). The parameter space of such calculations is large, including shock velocity, preshock density, ionization level and magnetic field, transverse dimension (radiative transfer parameter R_{max}), elemental abundances, completeness of the recombination region, and the grain component available for destruction.

For this effort the models were constructed as described in Cox (1972*a*) and Raymond (1979). The atomic rates used have been recently revised to include the large body of accurate cross sections made available in the past few years. These revisions are summarized in Cox and Raymond (1985). This latter paper also presents examples of the spectra of complete cooling flows and an approach to the analysis of spectra in families differing in their preshock ionization states. This approach reduces the need to calculate spectra for a complete range of preshock ionization fractions. We initially adopt the simplifying assumptions that the preshock magnetic field and density are too low to affect the spectra appreciably (0.1 μG, 2 cm^{-3}), that the transverse scale is large ($R_{max} = 3$), and that for the most part grains are evaporated so rapidly that their elements are in gaseous form immediately inside the shock front. The initial calculations are performed using normal abundances, log $N(Z)$ − log N(H) + 12 = 10.93 (He), 8.52 (C), 7.96 (N), 8.82 (O), 7.92 (Ne), 7.20 (Mg), 7.50 (Si), 7.20 (S), 6.90 (Ar), 6.30 (Ca), and 7.50 (Fe) (see Allen 1973). We will show below that a higher preshock density, a significant nonthermal pressure, and some depletion of the refractory elements are indicated.

Figure 8 shows the running integrals of the line strengths versus accumulated column density measured from the shock) for shock velocities of 80, 100, 120, and 140 km s^{-1}. In all but the 80 km s^{-1} case the gas was assumed fully preionized, so that these velocities are v_i in the notation of Cox and Raymond (1985). Cumulative line strengths relative to Hβ are on the left and fractions of the final line strengths are on the right. Use of column density as the measure of development is appropriate since the results are then independent of preshock density (so long as it is moderate and the magnetic field is weak). The plots in Figure 8 were taken from runs having the shock parameters listed in Table 7, in particular, higher density and magnetic field. Models having weak magnetic fields are quite similar, except that the column density scales for completion would be lower by nearly an order of magnitude.

Two features characterize the results. There is roughly a factor of 30 column density spread between significant accumulations of the first UV lines formed in the cooling region and the last optical lines from the recombination zone. In addition, the column density required for a given degree of completeness is *roughly* proportional to shock speed squared, with $10^{18.5}$ cm^{-2} appropriate for 100 km s^{-1} shocks approaching completion of their recombination regions. (These calculations assumed full preionization of both hydrogen and helium except for the 80 km s^{-1} model. The presence of H or He^0 would enhance the post shock cooling rate, decreasing the column densities required to reach a given maturity. Cox and Raymond [1985] showed that the effect was similar to that of lowering the shock velocity at full ionization.)

Considering the variety of conditions present in the Cygnus Loop, with shocks in both adiabatic and completely radiative regimes, the factor of 30 column density range for radiative but incomplete structures should be well represented. For example, the Hα bright nonradiative shocks with velocities around 150 km s^{-1} typically have $n_0 \sim 1$ cm^{-3} (Raymond *et al.* 1983). These should remain essentially nonradiative only to a column density of $10^{17.2}$ cm^{-2} ($\Delta R \approx 0.05$ pc/n_0, $\Delta t \approx 330$ yr/n_0) but then have incomplete recombination regions for another time period of several thousand years divided by n_0.

Incompleteness of a recombination region often has an obvious spectral signal, the ratio [O III]/Hβ exceeding the maximum available from complete structures. This ratio is small for slow shocks, which generate little [O III], and also fast shocks, where [O III] saturates but Hβ continues to rise. The maximum ratio for a fully developed flow with full preionization is about 6 for v_s between 80 and 140 km s^{-1}. Consulting

TABLE 7

SHOCK PARAMETERS FOR THE SPUR FILAMENT

	SE	M	NW
v_s(km s^{-1})	140	120	80, 100
n_0 (cm^{-3})	4.4	6.0	8.7
B_0 (μG)	11	15	17
log N_H (cm^{-2})	18.20	18.25	>18.6
Preshock H I	0.0	0.0	0.10, 0.01
Preshock He I	0.0	0.0	0.2, 0.0
Preshock He II	0.88	0.88	0.8, 1.0

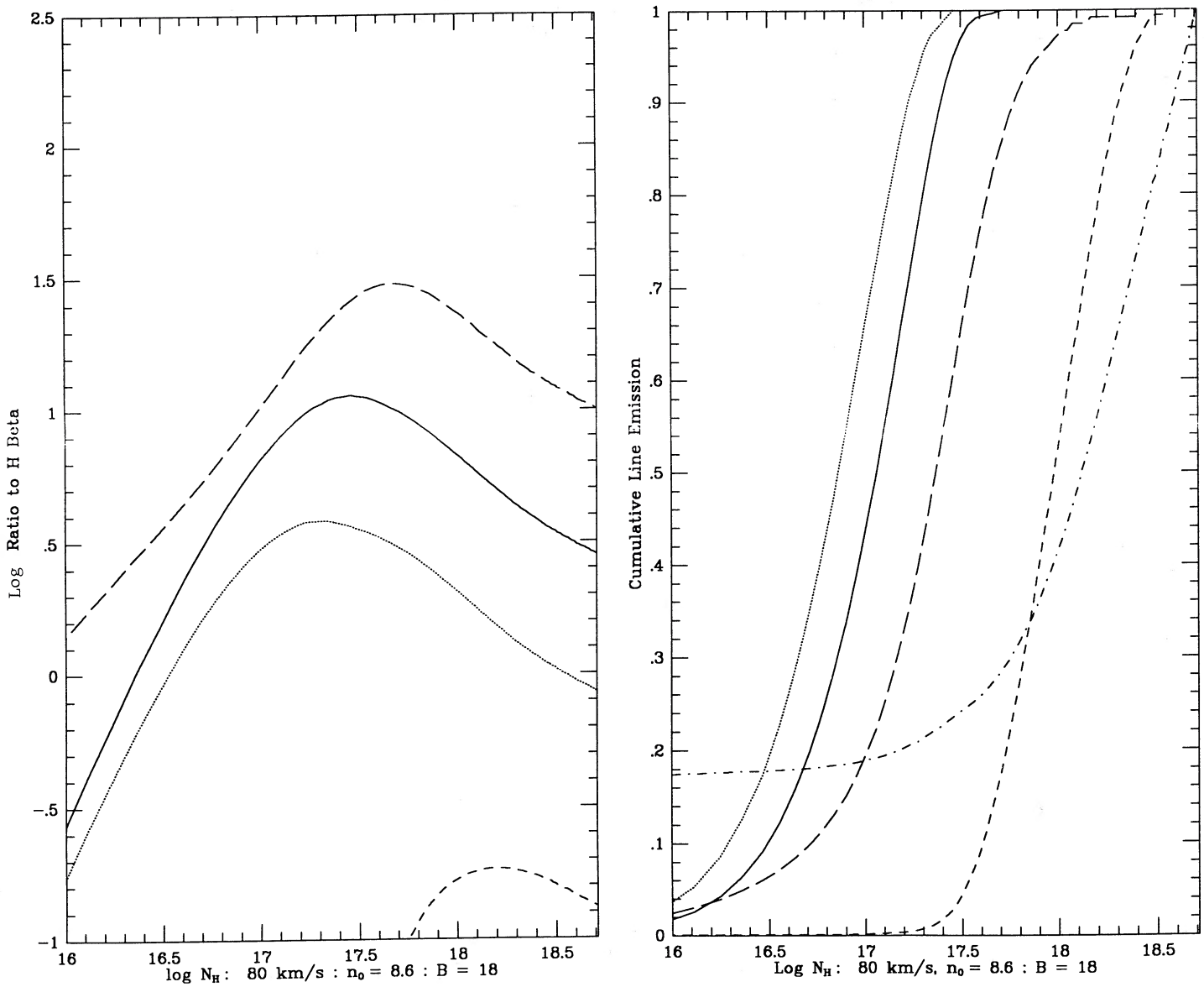

FIG. 8a

FIG. 8.—Emission structure of (*a*) 80, (*b*) 100, (*c*) 120, and (*d*) 140 km s^{-1} shocks, for parameters listed in Table 7. Left panels show log of line strength relative to Hβ: *dotted curve*—O III] $\lambda\lambda$1662, 1666; *solid curve*—[O III] $\lambda\lambda$4959, 5007; *long-dashed curve*—[O II] $\lambda\lambda$3727, 3729; *short dashed curve*—[O I] $\lambda\lambda$6300, 6363;

Figure 8, we see that this maximum is easily violated by shocks with incomplete recombination regions. It is also frequently violated by the observations (Fesen, Blair, and Kirshner 1982, 1985). A normal to weak [O I]/Hβ ratio assures that incompleteness rather than an overabundance of oxygen is the appropriate explanation.

Using truncated steady state structures for the model of the filament, there is a strightforward procedure for determining the shock velocity, preshock ionization, and accumulated column density. We notice first that if [O III] is prominent, the UV spectrum from the cooling region is essentially complete. Using UV line ratios between higher ionization stages, one determines the postionization enthalpy (or effective shock velocity in neutral or fully preionized gas). The ratios N V:N IV]:N III] and O IV]:O III] are especially useful for this, each using a single element. The strength of the two-photon continuum can then be used as per Cox and Raymond (1985) to solve separately for the preshock ionization fraction and the shock velocity.

Using the calculated spectrum for a complete cooling region with these parameters, one is then able to form ratios of observed to complete brightnesses for the optical lines arising from the recombination region. Finally, by mapping those ratios onto the corresponding completeness plot, one finds as many measures of the degree of completeness, the column density. To the extent that the various line ratios (measured to complete) agree, the accumulated column density is determined.

If the lines of C, N, and O are not matched by the above procedure, the abundances must be adjusted. When the shock parameters and abundances of the major coolants have been determined, the abundances of less common elements may be adjusted. This is straightforward in that the line intensities of all but the dominant coolants vary linearly with abundance.

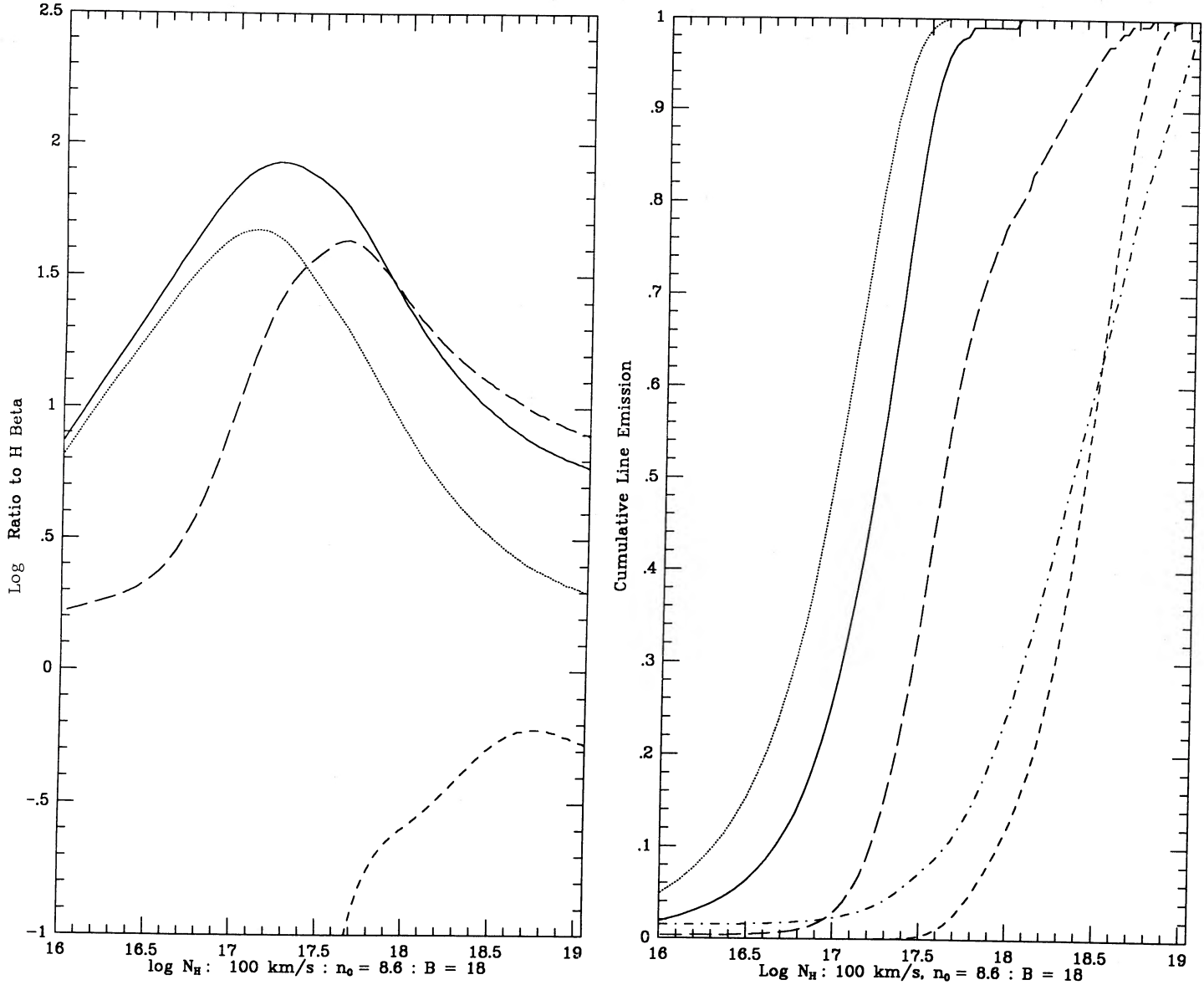

FIG. 8*b*

Finally, one can fine-tune the model with changes in preshock magnetic field, the radiative transfer parameter R_{max}, and the preshock density.

b) Surface Brightness and Doppler Shift Models

We now turn from models of the overall emission spectrum to models of the morphology and velocity structure of the spur. The most successful description of the optical emission of the Cygnus Loop assumes that it arises in large-scale sheetlike zones trailing radiative shock fronts. Modest inhomogeneities in the preshock medium cause the surface to be warped and bumpy on scales ranging from a few seconds of arc to the size of preshock interstellar clouds where the larger scale inhomogeneity is evident (typically in parsecs). Filaments are seen where the line of sight is tangential to the surface, while fainter diffuse emission is seen where the emissive sheet is viewed more obliquely. This description explains several aspects of the data, including the depth of filaments as inferred from the emission measure and electron density (Parker 1967; Miller 1974) and the similarity of the spectra of filaments to the spectra of the surrounding diffuse emission (HPD).

Two arguments have been advanced against the sheet interpretation. In S147, Kirshner and Arnold (1979) found higher densities in sharp, high–surface-brightness filaments than in diffuse filaments and no velocity difference between sharp and fuzzy filaments. Straka *et al.* (1986) found no anticorrelation between filament width and radio surface brightness. However, filament width and sharpness are poorly defined quantities. The spur itself is an excellent example. It appears wide and diffuse in Figure 3, but the set of images used to construct Figure 3 includes several short-exposure images in which it appears quite sharp and narrow. This can be easily seen by imagining what Figure 3 would look like if the lower two or three contour levels fell below the detection threshold. It is also worth noting that the radio observations which Straka *et al.* (1986) used as evidence against the sheet model are compatible

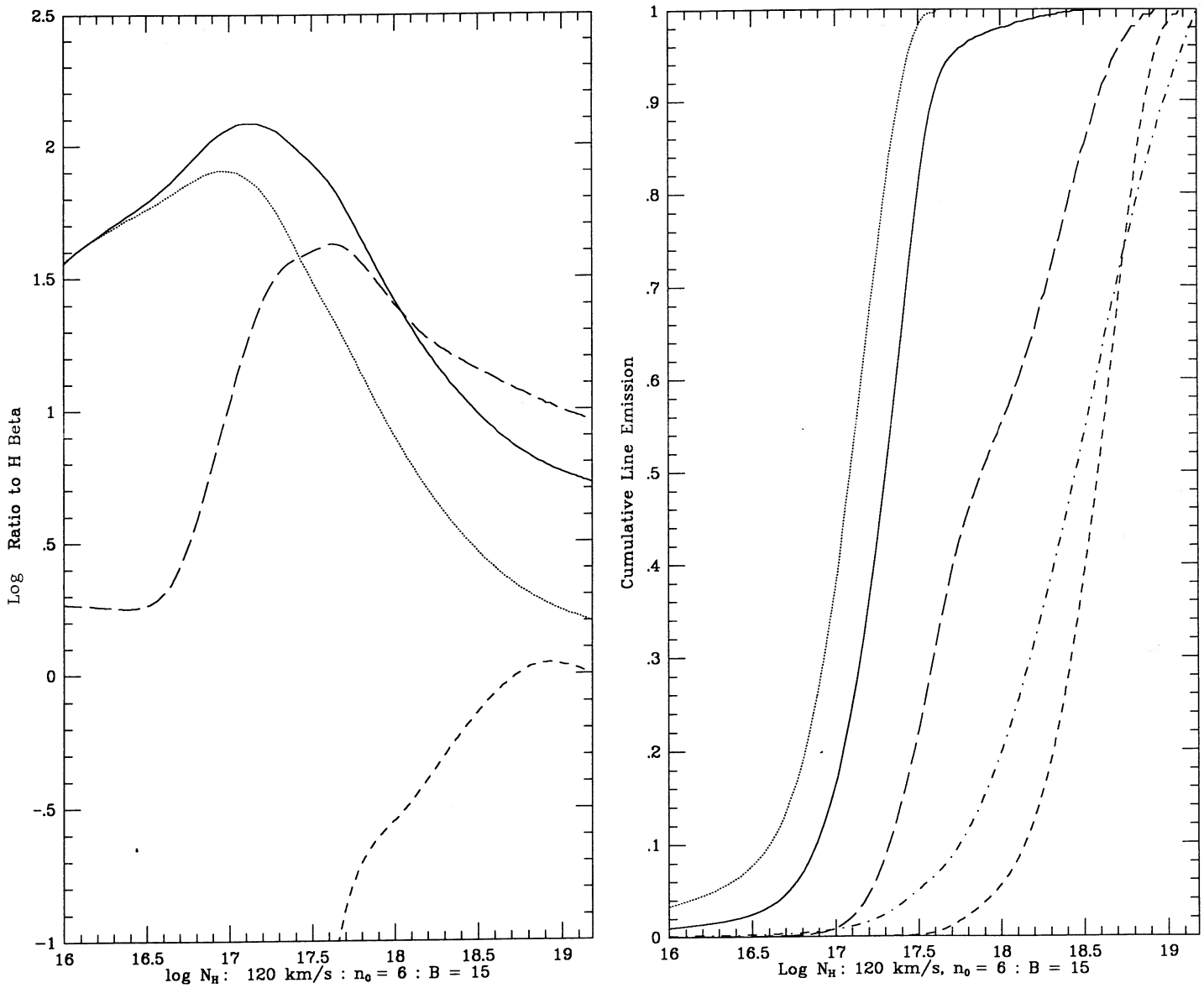

FIG. 8c

with a rippled sheet. For a uniformly emissive sheet with a simple geometry (such a sinusoidal ripple) the surface-brightness enhancements of the tangencies to the line of sight will be on the order of the filament separations. This means that the total luminosity will be roughly evenly divided between "filament" and "diffuse" components, exactly as observed by Straka *et al.* While detailed predictions are not available for ropelike geometries, one would expect that compression of both particles and fields in the ropes would lead to a far larger ratio of filament surface brightness to interfilament surface brightness.

Models of surface-brightness and velocity structures resulting from various sheet geometries have been presented by Hester (1987). These idealizations assumed a uniformly emissive shock of constant speed, its velocity everywhere normal to the front. These models show that shock fronts with line-of-sight geometries no more complicated than the projected geometries of observed filaments, and velocities like those inferred from filament spectral line ratios, will have complex velocity profiles quantitatively similar to those measured by Shull *et al.* (1982). Quite modest density inhomogeneities ($\sim$20%) can easily account for regions having the appearance of many filamentary features more or less parallel to each other, as in the northeast section of the Cygnus Loop. Large density contrasts cause features at sharp angles, such as the shocked cloud XA examined by Hester and Cox (1986). The spur itself is a smooth sheet, analogous to the northeast Cygnus Loop, but on a much smaller scale. The oblique orientation of the sheet to the local radius vector and to other bright filaments near it arises from the density enhancement centered at Miller's position 2 (see § IV*c*). Cuts across gently curved structures, such as the spur, will lead to the complex "multiple component velocity profiles" presented by Shull *et al.* (1982). They also unavoidably predict velocity widths of 0.1–0.2v_s for the level of filament contrast seen in the Cygnus Loop, in excellent agreement with the observations of Shull *et al.* (1982).

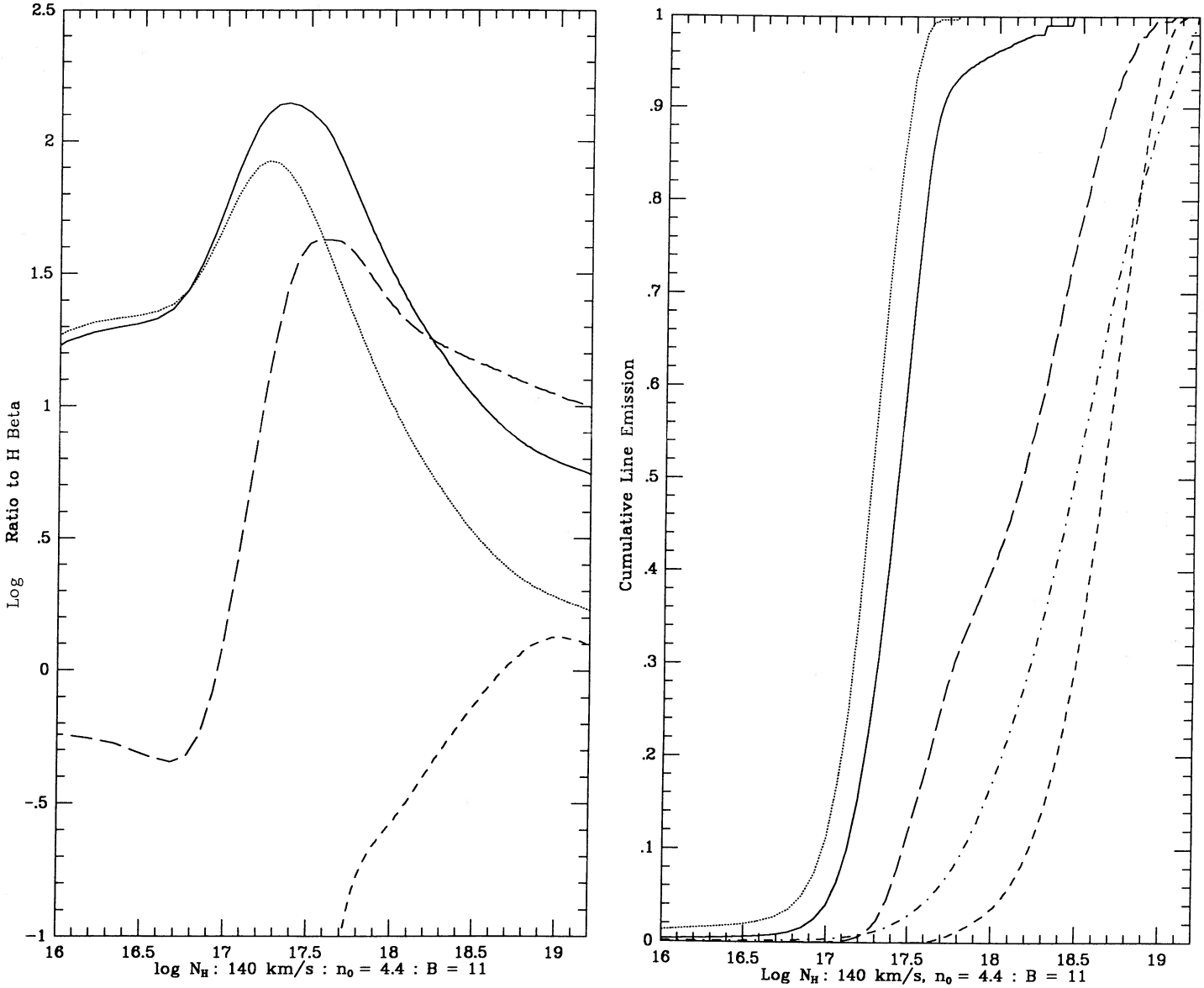

FIG. 8*d*

Geometries which involve small-scale structure, such as small dense clumps or ropes, are likely to have strongly curved shock fronts like those of the bow shocks seen in HH objects. This would imply velocity widths about equal to the shock velocity (Hartigan, Raymond, and Hartmann 1987).

The model idealizations can be disturbed by factors such as an uneven distribution of effective driving pressure, the presence of foreground or background emission, or even the very preshock density variations giving rise to the surface distortions. Although the essential features of the surface-brightness–velocity profile relation are not altered, this noise can make unique reconstruction of filament geometry impossible. There is, however, a characteristic of the relation that should distinguish it from other emission models whenever very deep, spatially resolved high-resolution spectra are available. Since the emission arises from a region with a smoothly varying velocity field that is contiguous in space, it should map into a contiguous structure in position—velocity space. Models in which the filaments are physically discrete from their surroundings (e.g., thermal instability models), or in which the velocity spread is due to random motions of "cells" of gas (Shull *et al.* 1982) would not show this continuity of structure.

We now consider the echelle spectrograms in Figure 6. The spur itself is quite prominent in the spectrograms as a very bright feature, indicating that it is an especially deep tangency to the line of sight. (This is what gives the spur the clean appearance that led us to choose it for further study.) Despite this, the spur is clearly part of a larger, continuous structure which includes the diffuse emission on both sides. This is most clear in [O III]. The LSR velocity of the brightness peak of the spur itself is -38 km s^{-1}, consistent with the velocity of the H I cloud in this part of the Cygnus Loop observed by DeNoyer (1975). This confirms that the shock velocity is perpendicular to our line of sight where the emitting surface is tangent.

The echelle data show that variations in spectral properties exist along the line of sight as well as along the length of the spur. Some components of the profile can be seen in both

[O III] and Hα plus [N II], while others are present only in emission from the high- or low-ionization species (just as some features appear predominantly in [O III] images, some in Hα images, and some in both). It is clear that the spectrum at any given point along the spur is a composite of emission from shocks with a range of parameters such as velocity and completeness. This adds an unfortunate, but unavoidable, complication to the interpretation of spectra from shocks. Additional morphological and velocity data can be of use in overcoming this difficulty. Slow variation of line ratios both along and across a filament could be used to choose a filament with little variation of shock paramenters along the line of sight.

IV. INTERPRETATION

A cursory inspection of the spectra in Table 5 shows essentially complete confirmation of the HPD expectations. There is a steady increase in the UV flux from northwest to southeast along this spur and a steady relative increase in the higher excitation lines. The normalization to Hβ hides a significant further confirmation. By comparing with [O III] instead, one notices that while the UV hardens and intensifies, the recombination seems to become less complete. The lines of [O I], [S II], [N II], and, to a lesser extent, [O II] become weaker. In addition, at position SE, the temperature sensitive ratio $I(4363)/I(5007)$ of [O III] rises slightly above the highest value appropriate for a complete cooling region, further supporting the interpretation of incompleteness. We will now use the models described in the previous section to determine the variations in the shock velocity, v_s, and completeness. The shock parameters we derive are emission-weighted averages over the portions of the emitting sheet within the *IUE* aperture at the three positions. This involves averaging both along the spur and along the line of sight.

a) Shock Parameters

i) *Shock Velocity and Preionization*

By comparing the relative fluxes of the three ultraviolet nitrogen lines and the two ultraviolet oxygen lines with shock models, we find the effective shock velocities; the shock velocities v_i which would give the observed UV emission line ratios in preionized gas (Cox and Raymond 1985). At position SE, a 140 km s^{-1} shock matches the ultraviolet N and O line ratios. At position M, the *IUE* spectrum was underexposed due to the slit orientation, so the measured fluxes are more uncertain. We take v_i to be 120 km s^{-1}, since higher velocity shocks predict too much O IV] emission, while lower velocities give too little N V. The differences between the optical spectra NW_a and NW_b show that the shock parameters change dramatically along the length of the *IUE* slit at position NW. From the presence of C IV and N IV] emission and the absence of N V, we estimate $v_i \approx 100$ km s^{-1} at the higher velocity end of NW. From the strength of the [O III] optical lines at NW_a we find a velocity between 65 km s^{-1} and 90 km s^{-1} for preshock ionization states ranging from fully ionized to 20% neutral. Combinations of somewhat higher v_s with higher preshock neutral fractions can also produce the observed [O III] strength, but, as discussed below, they predict unacceptably large Hα/[N II] ratios. Thus, for the model in Table 5, we take an unweighted average of 80 and 100 km s^{-1} shocks with 10% neutral hydrogen (see below) in the preshock gas for the 80 km s^{-1} model. The uncertainty of the velocities at SE and M is about ±10 km s^{-1}, while the uncertainty at NW is a little greater owing to the sensitivity to the preshock ionization conditions.

A shock in partially neutral gas resembles a lower velocity shock in fully ionized gas. Cox and Raymond (1985) suggest the use of the UV two-photon continuum and, for complete structures, the [N II]/Hα ratio to infer the preshock neutral fraction. Using their models and the ratio of two-photon continuum to Hβ, we find that the preshock gas is fully ionized at all three positions. While the uncertainty in the strength of the two-photon continuum is rather large, the strengths of such optical lines as [N II] and [O II] relative to the Balmer lines confirm the high preshock ionization state of the gas. We estimate the upper limit on the preshock neutral fraction of hydrogen to be 20%. We therefore assume full preionization at SE and M. The ratio of two-photon continuum to Hβ tends to be low in the low-velocity shocks due to the relatively low temperature of the recombination zone. A significant neutral fraction would improve this ratio, but it would cause problems with the [N II]/Hα ratio, which is more reliably determined from the observations. We take a 10% neutral fraction for the 80 km s^{-1} shock, but anything below 20% is allowable.

The full ionization of the preshock gas is not surprising for the M and SE positions, as the shock velocity is high enough for each hydrogen nucleus passing through the shock to produce more than one hydrogen ionizing photon emerging through the front. However, the NW shock is too slow to produce full preionization in steady state. The equilibrium condition according to Shull and McKee (1979) and to our own models is a preshock neutral fraction between 92% and 32% for shocks in the 80–100 km s^{-1} range. The NW preshock ionization state is clearly not in equilibrium with the present shock velocity. This is less surprising than it might seem in that the recombination time for gas at a density of 6 cm^{-3} (see below) is 17,000 yr, or roughly the entire age of the Cygnus Loop. The shock at position NW probably slowed from a higher velocity in the recent past due to a combination of increasing preshock density and decreasing ram pressure as the Cygnus Loop blast wave swept past (see McKee *et al.* 1986; Hester and Cox 1986). During that slowing down it would have produced ionizing photons which could ionize the gas which the shock is now reaching. In any event, the very long recombination time of hydrogen at densities near 1 cm^{-3} compared with the ages of supernova remnants bright enough to be observable leads us to expect that many 50–100 km s^{-1} shocks in supernova remnants are traveling in fully ionized gas. Cox (1972*b*) found this result for a supernova remnant in a homogeneous medium, and it is apparently true for inhomogeneous media as well, as long as the decrease to velocities below 100 km s^{-1} is continuous. The preionization of the spur sheets cannot be a relic of a flash of photons from the supernova outburst itself. *The large neutral fraction required to understand the nonradiative Balmer line filaments shows that, even down to* $n_0 \sim 1$ cm^{-3}, *material is not fully preionized until after formation of the cooling region.*

The preshock ionization state of helium is not reliably known. Radiative transfer calculations in the He^+ λ256 line will be needed to determine the preshock ionization state of helium from the λ1640 intensity. If the preshock helium were entirely doubly ionized, the shock velocities at positions M and SE would be reduced by 5–10 km s^{-1}.

ii) *Resonance-Line Scattering*

Having established the shock velocity and preshock ionization state, we pause to consider the C II and C IV lines, which

are predicted to be very bright and seem like useful diagnostics of carbon abundance and shock velocity. They are, unfortunately, useful only as upper limits due to the effects of resonance-line scattering in the filament itself (Raymond *et al.* 1980, 1981). This is due to the edge-on sheet geometry of the filament. The optical depth of the C IV resonance doublet is near 0.5 in the direction normal to the shock surface, and along the line of sight it is much larger. The *IUE* spectrum of position M provides a direct test of the scattering hypothesis. As one moves away from the brightest portion of the filament, the C IV surface brightness should remain constant until the angle between the sheet of emitting gas and the line of sight becomes large enough for the C IV optical depth to fall below one. This expectation is confirmed by SWP 23774, the spectrum in which the Large Aperture was aligned perpendicular to the spur. In C III] λ1909, the spur shows up as a bright ridge crossing the center of the aperture, but in C IV the slit is uniformly filled, as computed by summing each of the *IUE* line-by-line spectra over 10 Å at each line. The ratio of C IV to C III] intensities is 0.50, 0.25, and 0.51 for the sections of the Large Aperture located north of, centered on, and south of the spur, respectively. Slower shocks produce weaker C IV emission, but the optical depth of the C IV line is also smaller. Thus we expect that the attenuation of the C IV flux by resonant scattering is less severe for position NW than for the other positions. Indeed, the C IV flux observed there is much closer to the predicted value.

Further confirmation of the resonant scattering interpretation for the weakness of the ultraviolet resonance lines comes from the low observed ratios of the permitted C II λ1335 line to the intercombination line at λ2325 (Table 5). The other strong resonance lines in our spectral range affected by resonant scattering are the N V λ1240, Si IV λ1396, and Mg II λ2800 doublets. If we attribute the difference between predicted and observed C IV intensities in Table 5 to resonant scattering, the optical depths in the C IV doublet can be crudely estimated from escape probabilities to be 7 and 3.5 at position SE. The model predictions for the column densities of C IV and N V then imply optical depths of $\sim$1.0 and 0.5 for the N V lines and an attenuation of the N V emission by $\sim$40%. The large oscillator strength of the Si IV doublet makes it more susceptible to resonant scattering, with optical depths of 2 and 1, for attenuation by more than a factor of 2. The shock models predict that Si IV contributes around 30% of the intrinsic emission in the λ1400 blend, but since this contribution is reduced by at least a factor of 2 by scattering within the filament and in the intervening interstellar medium, we do not include the Si IV contribution to the λ1400 predicted fluxes in Table 5. Likewise, the Mg II doublet is expected to be severely attenuated by scattering within the filament, then further reduced by strong interstellar absorption.

iii) *Preshock Density, Ram Pressure, and Nonthermal Pressure*

Having found v_s, we may determine the preshock density. The standard procedure is to measure the electron density in the recombination zone from the [O II] or [S II] doublet ratio, then divide by the compression expected for the shock velocity determined above. The danger of this procedure lies in the tacit assumption that gas pressure dominates magnetic and cosmic-ray pressure in the recombination region. In fact, for typical interstellar densities and magnetic fields, magnetic pressure probably dominates in the recombination zone. The strong dependence of the shock compression on the shock velocity and the difficulty of accurately measuring the electron density near the high- or low-density limits of the doublet ratios present further problems.

The long slit echelle data between positions M and NW and the absolute surface-brightness maps permit a more direct ram pressure measurement (Cox, Hester, and Raymond 1987). This method makes use of velocity data just off tangency to infer an orientation of the emitting surface and therefore the enhancement factor in its surface brightness due to that orientation. The formal (face-on) surface brightness of the sheet thus found is compared with shock models at the previously determined shock velocity. The value of n_0 is that needed to provide the face-on surface brightness. After finding n_0 through this approach, we shall show that the method actually provides a very good measure of the ram pressure ρv_s^2, independent of accurate knowledge of v_s.

The [O III] echelle image in Figure 6 shows that $\sim$11″ south of the surface brightness peak of the spur the emission splits into components having radial velocities , v_{obs}, of +28 and -15 km s^{-1} relative to the surface-brightness peak. The -15 km s^{-1} component is drastically incomplete, as judged by the lack of [N II] and Hα at that velocity in Figure 6*b*, while the +28 km s^{-1} component is complete at least through the [O III] emission region. The probable incompleteness of even the [O III] emission in the -15 km s^{-1} component makes its interpretation difficult without further data, so we will ignore it. The shock velocity is $\sim$110 km s^{-1}, intermediate between the values for positions M and NW. The angle between the line of sight and the emitting sheet must be 15° to have radial velocity 28 km s^{-1}. The surface brightness of this component is determined by dividing the [O III] surface brightness at this location from the HPD map (8.7×10^{-5} ergs cm^{-1} s^{-1} sr^{-1}) into components according to the relative intensities of the +20 and -15 km s^{-1} components in the echelle data. This procedure yields 5.9×10^{-5} ergs cm^{-2} s^{-1} sr^{-1} for the -28 km s^{-1} component. Since the line of sight cuts the emitting sheet at 15°, the face-on surface brightness of the sheet must be 1.5×10^{-5} ergs cm^{-2} s^{-1} sr^{-1}. This surface brightness is simply proportional to n_0 at a given shock velocity, and, from the models of the previous section, we find $n_0 = 8.0$ cm^{-3}. The uncertainties are $\sim$25% from the surface brightness, 20% from the velocity, and 20% from the model, for an overall uncertainty of $\sim$40%.

The ram pressure $\rho_0 v_s^2$ is 1.9×10^{-9} for $v_s = 110$ km s^{-1}. It turns out that most of the uncertainties in its determination cancel (Cox, Hester, and Raymond 1987). The face-on and observed surface brightnesses and velocities are related by

$$\frac{v_{obs}}{v_s} = \frac{I}{I_{obs}} \tag{1}$$

or

$$v_{obs} I_{obs} = v_s I \, . \tag{2}$$

The normal surface brightness of the shock can be written as the number of H atoms swept up per second times the number N, of [O III] photons emitted per average atom in the cooling flow. Thus,

$$v_{obs} I_{obs} = n_0 v_s^2 N \frac{h\nu}{4\pi} \text{ ergs cm}^{-1} \text{ s}^{-2} \text{ sr}^{-1} \, , \tag{3}$$

where $h\nu$ is the photon energy. The ram pressure, $\rho_0 v_s^2$, is uniquely determined by the two observed quantities, the value

of N determined from the shock models and the mean atomic weight of the gas. Fortunately, the number of λ5007 photons per average atom is a very slowly varying function of v_s for shocks faster than 80 km s^{-1} in ionized gas or 110 km s^{-1} in gas with equilibrium preionization. The value of N does depend on the elemental abundances, but the UV and optical spectra allow us to constrain the abundances tightly. For shocks in ionized gas, N ranges from 0.5 to 0.8 for $v_s > 80$ km s^{-1}, and 0.55 ± 0.05 is the range appropriate to the shock parameters for position M. With the mean atomic weight appropriate to the abundances listed in § III, the ram pressure $\rho_0 v_s^2$ is again 1.9×10^{-9} dynes cm^{-2}.

Cox, Hester, and Raymond (1987) analyze the long-slit echelle spectrogram by measuring v and I at nine separate positions along the redshifted component south of the spur. The product $v_{obs} I_{obs}$ varies by only 20% over the structure, with the value quoted being one of the larger ones.

The thermal pressure in the recombination zone can be determined from the [S II] ratio. As discussed by Cox, Hester, and Raymond (1987), this is difficult close to the low-density limit, but from a high quality spectrum they found electron densities ranging from 20 cm^{-3} in the NW to 75 cm^{-3} in the SE. The value at M was 20 cm^{-3} with a formal error of ± 6 cm^{-3}, but such a low density has unacceptable consequences. In particular, the thickness of the emissive region should exceed that observed on the sky. We regard $n_e \sim 40$ cm^{-3} as essentially a lower limit consistent with the observed thickness. It is also marginally consistent with observations when uncertainties in the atomic physics are included. Because of incompleteness, the gas is largely ionized in the [S II] zone, so the corresponding thermal pressure is 1×10^{-10} dyn cm^{-2}; we are attempting to obtain the [O II] doublet ratio to confirm this.

Our ram pressure measure thus exceeds our estimate of the thermal pressure in the recombination zone by an order of magnitude. We tentatively conclude that nonthermal pressure dominates by a large margin in the recombination zone. Our estimate of the total compression factor is roughly 7–15. As we show later, the X-ray surface brightness in this region of the Loop can also be used to estimate the pressure behind the shock. The upper bound on such estimates seems to be 6×10^{-10} dyn cm^{-2}, a factor of 3 lower than our ram pressure estimate. The differences among these three pressure measurements are capable of stimulating a rather considerable discussion over physical causes (Cox, Hester, and Raymond 1987; § IV*c* below), so let us now consider possible sources of error in the ram pressure.

It is important to note that the vI method for estimating ram pressure is basically just energy conservation: the number of [O III] photons per average atom passing through the shock reflects the fact that the cooling gas must radiate away a given amount of energy to pass through the [O III] temperature range, and the fraction of that energy which emerges in the [O III] line is not very sensitive to details of the shock structure. On the other hand, unresolved spatial structure in the emitting sheet can lead to an enhanced I_{obs} without changing the mean v_{obs}. It would, however, lead to an increased line width. Based on our successful modeling of the line width structure (§ IV*b*) that effect cannot have enhanced our pressure estimate by more than a factor of 1.5.

The sheet surface brightness may also exceed that of steady flow if the shock is decelerating significantly in one cooling time. The longer cooling time for a higher shock speed can leave some material from an earlier time lingering at [O III] emitting temperatures, while some very recently shocked material has already cooled to the [O III] temperature range. Such an enhancement is probably a short-lived phenomenon which would skew the [O III] to the UV lines sufficiently for the skewing to be readily noticeable. Considering the agreement of the relative optical and UV line strengths with the truncated shock models, we believe this effect to be small but an overestimate of $\rho_0 v_s^2$ by a factor of 1.5 cannot be ruled out.

In deriving the preshock density using the vI method, we have assumed that the entire surface of the emitting sheet is contributing to the emissivity. If only a fraction f of the shock surface is emissive, on an unresolved scale, then the preshock density in those regions is of order $7/f$ cm^{-3} in order to achieve the observed surface brightness. The ram pressure is then also increased by f^{-1} over our earlier estimate, enhancing the disparity we are exploring.

In summary, the uncertainties we are exploring are roughly 40% total from measurement, a factor of 1.5 from unresolved structure, and another factor of 1.5 due to transient overbrightness following rapid deceleration. Since two of these uncertainties would systematically lead to overestimates of the ram pressure, we should probably be accurate in quoting the ram pressure as 1.5×10^{-9} dyn cm^{-2} within a factor of 2.

There are at least three possible contributions to a difference between recombination region thermal pressure and the overall ram pressure. They include transient low pressure in a rapidly cooling region, as well as potential contributions of magnetic fields and cosmic rays to the total pressure. Blair, Kirshner, and Chevalier (1982) suggested that magnetic pressure limits the compression in the M31 supernova remnants they observed, and Chevalier (1983) pointed out that a plausible cosmic-ray pressure could also account for those observations. A transverse preshock magnetic field of ~ 30 μG is required to limit the compression at position M so severely, far higher than the mean interstellar field. Models for cosmic-ray acceleration by shocks of this kind are highly variable in the amount of acceleration predicted, but it is clear from the high cosmic-ray pressure needed in the recombination zone that great efficiency for conversion would be needed. If acceleration of ambient cosmic rays occurs, the pressure enhancement is roughly a factor of 4000, the density enhancement 10, for a mean energy amplification of 400. If most of the cosmic-ray pressure derives instead from newly injected particles, we infer that the downstream energy flux is $3p_{CR} v_s/X$, where X is the overall compression factor, ~ 10. Since we infer that $p_{CR} \sim \rho_0 v_s^2$ and that the total incoming energy flux is $\rho_0 v_s^2/2$, we find that the total conversion efficiency to cosmic rays is roughly $6/X \sim \frac{1}{2}$, which is in fact a prediction of some theories (e.g., Eichler 1985) (see note added in manuscript).

For the spectral studies of the present paper, it doesn't much matter what takes over the pressure, so, in constructing model spectra, magnetic fields were used to limit the compression. On the other hand, what the UV lines measure is the postshock temperature, rather than shock velocity; with significant conversion to nonthermal energy, a higher shock speed and correspondingly lower n_0 may be needed to achieve that temperature at the measured ram pressure. These effects are small, however, as seen from the adequacy of the spectral models presented below.

We have a preshock density determination only for the long-slit echelle position. It is plausible to assume constant ram pressure along the spur to estimate n_0 for the other positions, but we cannot test this assumption with the present data. We also assume that the effective preshock magnetic field goes as

$n_0^{0.5}$, but this is also untested. These assumptions have very little effect on any of the parameters derived for the shocks at these positions except for the column densities, which are discussed in the next section.

iv) *Column Density*

Now that the shock velocity and preionization have been established, the completeness of the shock can be estimated as described earlier. The ratios of oxygen lines to Hβ are compared with Figure 8 to find log (N_H) values of 18.2, 18.30, and >18.6 for SE, M, and NW, respectively. These column densities are affected by the assumed magnetic fields. They would all be ~ 4 times smaller in the limit of negligible field. The agreement of the ratios of the three optical oxygen lines to Hβ for a single value of N_H at SE and M is remarkably good, confirming that truncation of the shock is a reasonable approximation to the nonsteady flow. Other lines, particularly [S II] and [N I] are also matched quite well by the truncated shock models. The specific truncated models used to match the spectra are listed in Table 7 and compared with the observed spectra in Table 5. No adjustment of the abundances of the major coolant species is necessary.

v) *Elemental Abundances and Grain Destruction*

With the shock parameters and the abundances of the dominant coolants determined, abundances of the less common elements can now be adjusted as necessary. As seen in Table 5, the standard abundance set provides good agreement for most of the lines. The predicted [Ne IV] intensity seems systematically too large, while the [Ne III] prediction is too small, suggesting that the Ne IV recombination rate is underestimated. A low-temperature dielectronic recombination rate for Ne IV computed by Nussbaumer and Storey (1986) reduces, but does not eliminate, the discrepancy. The argon line agrees with the standard abundance prediction. The Si III] line at 1890 Å is predicted to be stronger than observed by about a factor of 2 with standard abundances. This may indicate a real depletion of silicon, though observation of some other silicon lines would be needed to make a convincing case. The [Fe III] line at 4658 Å is also observed to be a factor of 4 below the model prediction with cosmic abundances at position NW, and the failure to detect the line at SE and M strongly suggests that it is weaker than predicted there as well. If the apparent depletions of Si and Fe with respect to O and N are correct, they agree reasonably well with the grain destruction models of Seab and Shull (1983), though McKee *et al.* (1986) show that a magnetic field strong enough to limit the shock compression substantially reduces the destruction of silicate grains. Carbon seems not to be depleted at all with respect to oxygen and nitrogen, while the Seab and Shull models show it to be depleted by a factor of 3 even after grain processing. It may be that the initial factor of 5 carbon depletion assumed by Seab and Shull is much more severe than is appropriate for the Cygnus Loop. Raymond *et al.* (1983) found that carbon was only depleted by a factor of 2 in the gas encountered by the nonradiative shock in the northeast region of the Cygnus Loop. It is also possible that the carbon-bearing grains are fluffy, easily sputtered structures, rather than the solid graphite particles assumed in the dust destruction calculations.

b) Sheet Geometry

The line-of-sight geometry of the shock front was constructed from the long-slit echelle spectra under the assumption of constant shock velocity of 100 km s^{-1}. The emission was assumed to come from two components, one primarily redshifted and one blueshifted, which appear together in projection. The blueshifted component appears only in [O III], corresponding to drastically incomplete recombination.

The two components were reconstructed separately by idealizing the echelle data as a thin continuous line and then integrating

$$\frac{dy}{dx} = \left[\left(\frac{v_s}{v_{\rm obs}}\right)^2 - 1\right]^{1/2} \quad (4)$$

to get the geometry. This technique is unique for well-resolved structures such as the "split" to the south of the spur, but is not unique for true tangencies such as the spur itself. It is also insensitive to unresolved structure in the sheet that can broaden the line. As a check on the procedure, a velocity structure was determined from the inferred geometry in the manner described by Hester (1987) for comparison with the original data. Finally, the brightness of the sheet was varied along its length to obtain separate models for [O III] and [N II] plus Hα.

The results are shown in Figures, 9, 10, and 11. Figure 9*a* shows the geometry of the redder component, with brightness variations to match the Hα spectrum (shown to the lower right) indicated by the boldness of the line. The arrows show the shock velocity at several points along the sheet. Figure 9*b* shows the model spectrogram derived from the geometry shown in Figure 9*a*. It should be compared with the observations in Figure 6*b*, The labels along the spectrum correspond to labels along the sheet and show the correspondence between the geometry and features in the spectrum. Figure 9*c* shows the same geometry with brightness variations to match [O III]. Figure 10 shows the geometry of the blueshifted component. Figure 11 shows a superposition of the velocity structures derived from the geometries in Figures 9*c* and 10. The comparable observations are in Figure 6*a*.

The red component of the emission associated with the spur has a depth of ~ 2 pc along the line of sight. This extent depends somewhat on the assumed shock velocity and on the depth of the actual spur tangency (which could not be uniquely reconstructed). A lower shock velocity for the Hα-prominent emission north of the spur and a shallower tangency would bring the depth down somewhat, but nonetheless a depth in excess of 1 pc is indicated. This depth exceeds the entire length of the spur by at least a factor of 3. This might seem unlikely, except that the fact that the spur is such a clean and well-defined filament led to its selection for detailed study.

The inferred structure along the line of sight closely resembles the structure the length of the spur. The "kink" at the south end of the slit looks a lot like the kink at the southeast end of the spur where the filament turns sharply and tails off to the south. Similarly, the strength of [O III] relative to Hα generally decreases moving along the sheet away from this kink. The E–W bar across the field in Figure 1 ties into this structure at its north end. The increase in [O III]/Hα from west to east along the bar is another manifestation of this same trend of increasing v_s and decreasing completeness with distance away from the bright Miller 2 region. The Hα plus [N II] model does not reproduce a weak component near zero velocity in Figure 6*b*, which might be due either to photoionized material ahead of the shock or to Galactic background emission.

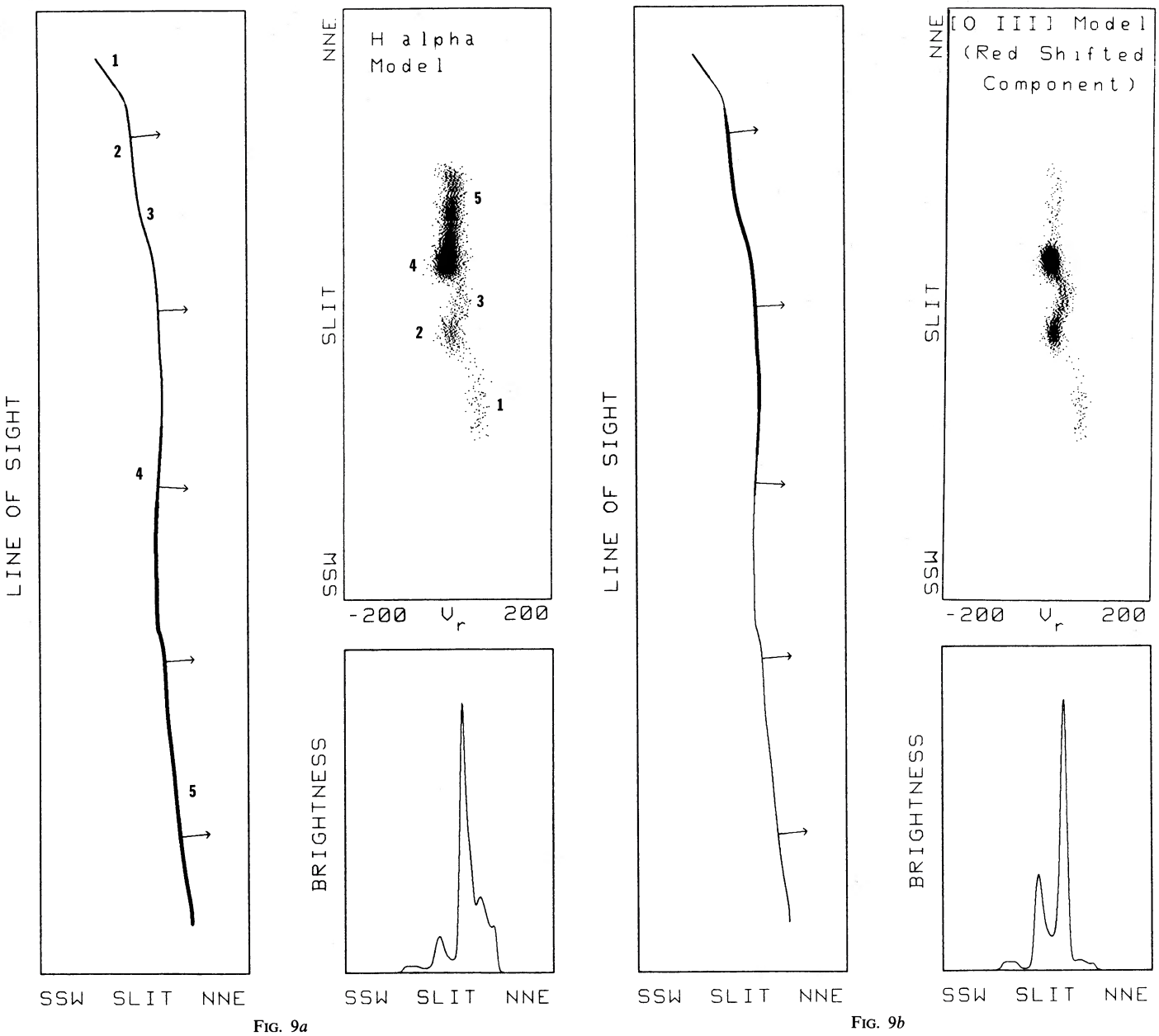

FIG. 9a FIG. 9b

FIG. 9.—(*a*) Geometry for redshifted component of Hα. Shock velocity is assumed to be 100 km s^{-1}, and emissivity variations are indicated by boldness of line. Predicted surface brightness as a function of position along the slit is also shown. Long-slit echelle image predicted from sheet geometry is shown with labels corresponding to those on the diagram of the geometry. (*b*) Geometry and surface-brightness distribution derived for redshifted component of [O III].

c) Shock History

Having extracted the shock parameters at the three positions observed, we now ask what ISM morphology could explain the observed structure. In keeping with current understanding of the interaction between SNR blast waves and interstellar clouds, the spur could be a somewhat flattened section of a converging conical shock, whose apex is the bright knot where the spur intersects Miller's (1974) position 2. The line profiles at positions SE, M, and NW (Fig. 5) all have about the same width, in spite of the increase in shock velocity from NW to SE. This requires that the curvature of the emitting sheet be stronger at NW than at SE, as expected from a conical geometry. A series of fainter filaments which stretches northeast from the knot where the spur meets Miller's position 2 can be seen in Figure 4 of HPD, and this could be the other limb of the cone.

The straightness of the spur indicates that v_s is proportional to the distance r from the apex, though the spectral data show a somewhat slower variation. We should, in any case, expect a reasonable consistency between the measured n_0, column density, and the observed distance of shock advance, shown through the closing angle of the cone. The distance of progression varies along the spur, but is of the order of 10^{18} cm for position M. The preshock density then indicates the expected column density to be $\sim 6 \times 10^{18}$ cm^{-2}. The truncated spectrum model yields roughly (Table 7) 2×10^{18} cm^{-2} in what must be considered spectacular agreement given the crude

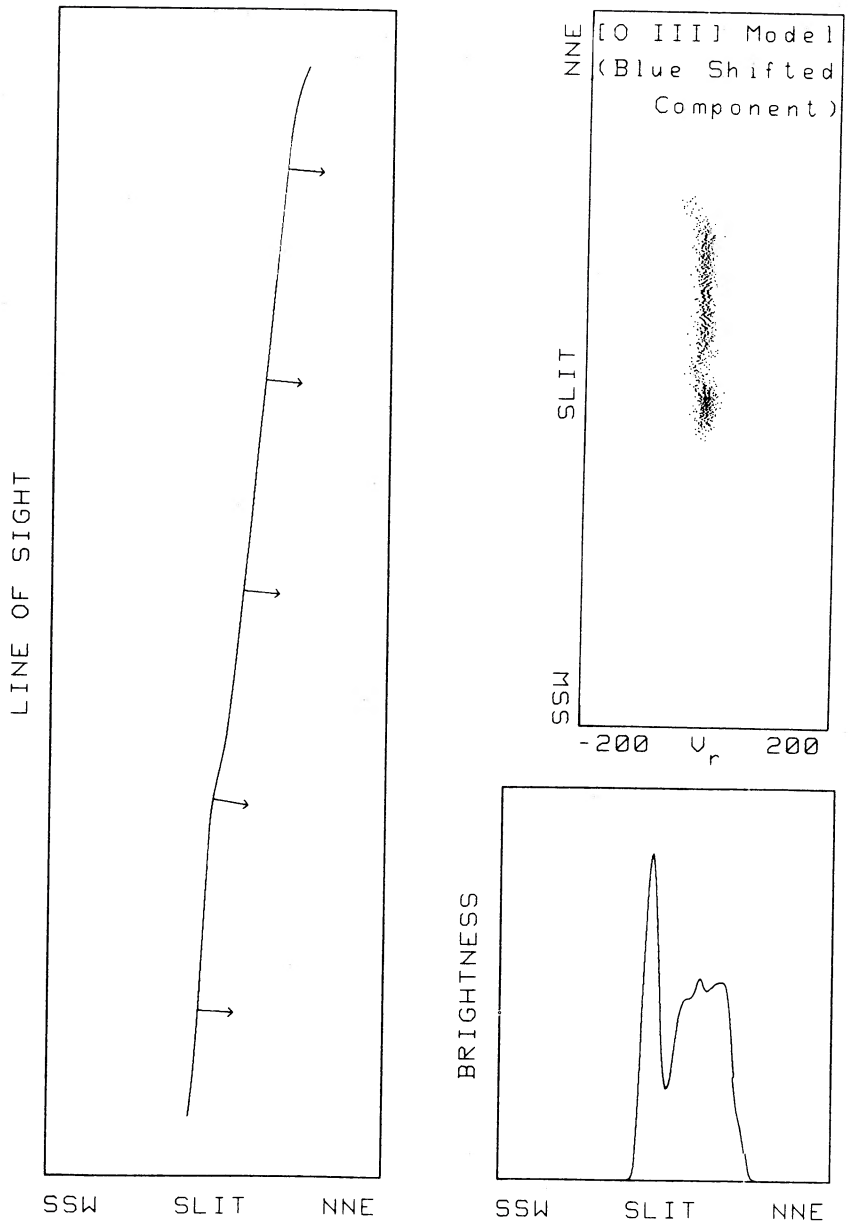

FIG. 10.—Geometry and surface-brightness distribution derived for blueshifted component of [O III]

assumption of constant density and the unknown initial geometry of the cloud.

The time required for the shock to close the cone to the observed angle is about 1350 yr, but by one-third that age it would acquire the observed column densities. As discussed by Hester and Cox (1986), the lack of enhanced X-ray emission from the vicinity of Miller's position 2 suggests that the overpressure near the stagnation point at the apex of the cone has had time to dissipate. This requires roughly the size of the dense cloud divided by the sound speed of the X-ray–emitting gas, or about 300 yr. Thus it is plausible that the region of Miller's position 2 and the HPD spur is a more evolved version of XA, the bow shock structure further west examined by Cox and Hester (1986).

It is noteworthy that the ram pressure of 2×10^{-9} dyn cm^{-2} which we derive at position M is more than 5 times the ram pressure inferred for the average X-ray–emitting gas in the Cygnus Loop (Ku *et al.* 1984). F. Seward has kindly measured the surface brightness and spectrum of a 2′ radius circle about position M from an *Einstein* IPC observation. The best-fit temperature is 3×10^6 K, typical of the bright portions of the Cygnus Loop (Ku *et al.* 1984; Charles, Kahn, and McKee 1985). The surface brightness implies $n_e = 1$ cm^{-3} if the depth of the X-ray–emitting region is 1 pc. This is about the line-of-sight depth of the spur, so it is a lower limit to the actual depth of the X-ray–emitting region. The pressure could therefore be as much as a factor of 3 lower than the value 4×10^{-10} dyn cm^{-2} which corresponds to a density of 1 cm^{-3}. On the other hand, recent *IRAS* observations (Braun and Strom 1986) show a great deal of dust in the X-ray–emitting regions of the Cygnus Loop. If we take this as an indication of severe depletion of the refractory elements (Mg, Si, and Fe being most

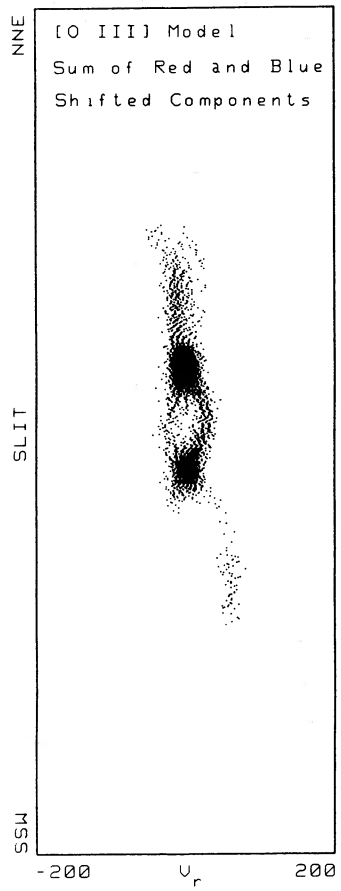

FIG. 11.—Long-slit echelle image predicted from sum of redshifted and blueshifted [O III] components.

important), the current version of the Raymond and Smith (1977) spectral code shows a factor of 2 reduction in the emissivity in the IPC band. Thus, the thermal pressure needed to account for the observed X-rays would be increased by 40%. Overall, the thermal pressure of the X-ray–emitting gas driving the spur shock is 2–12 times lower than the ram pressure of the shock itself. The thermal pressure in the recombination zone is only 1×10^{-10} dyn cm^{-3}, at the lower edge of the range of X-ray pressures, and a factor of 15 below the ram pressure. It is possible that the discrepancy. between the ram pressures of optical filaments and X-ray–emitting gas is a common feature which has been masked by magnetic support of the recombination region, though again our selection of a relatively bright filament for study has introduced a strong bias toward high–ram pressure regions.

The observation of a shock ram pressure higher than the pressure of the X-ray–emitting gas raises the question of what drives the shock. It is conceivable that the thermal pressure of the X-ray–emitting gas is only a small fraction of the total pressure there. Since the X-ray–emitting gas has not been compressed beyond the immediate postshock density, its magnetic pressure is unlikely to be significant. Some estimates of the pressure of accelerated cosmic rays are as high as 50% of total pressure at the shock, however (Eichler 1985). This interpretation would imply a substantially higher shock velocity to achieve the observed X-ray temperature. The higher velocity would mean a smaller age for the SNR. A higher shock velocity would also imply proper motions of the Balmer line filaments which might be unacceptably large (see Hester, Raymond, and Danielson 1986).

It is also possible that the pressure of the X-ray gas really is too low to drive a shock at the presently observed ram pressure. When an SNR blast wave encounters a dense cloud, a reflected shock brings the hot interior gas to rest and a temporary overpressure results (McKee and Cowie 1975; Heathcote and Brand 1983; Hester and Cox 1986). This overpressure can be a factor of 3–6 above the typical SNR pressure, but it dissipates over roughly 1000 yr, depending on the scale of the cloud hit. In the meantime, however, the radiative shock in the cloud has accumulated a substantial amount of material, and the momentum of this material can drive the shock just as it does in the "snowplow" phase of SNRs in homogeneous media. McKee *et al.* (1986) present methods for computing such a structure, but the result is likely to be sensitive to the assumed density structure of the cloud. If the shock ram pressure is supplied by momentum of the accumulated material, the difference between ram pressure and thermal pressure measures the sum of nonthermal pressure and the gradient of the momentum flux. One ought to find that future measures of the ram pressure along the spur would show the greatest disparities between ram and thermal pressures where the recombination region is most complete. As the [S II] lines are formed throughout the low-temperature region of the flow, about half the [S II] emission originates in the first half of the column density behind the shock. Therefore, we expect that if the gradient of the momentum flux dominates the pressure, the [S II] lines should show a thermal pressure on the order of half the ram pressure. Since the observed thermal pressure is at most 10% of the ram pressure, we conclude that nonthermal pressure dominates.

V. SUMMARY

Comparison of optical and UV line intensities and spatial and spectral optical line profiles of a well-defined Cygnus Loop filament with theoretical models shows that (1) the sharp filament is due to the tangency of a large, thin sheet of emitting gas to the line of sight, (2) the emitting region associated with the spur is very deep, (3) there is a substantial gradient in shock velocity along the filament, (4) severe incompleteness of the recombination zone is found at the high-velocity end, (5) resonant scattering in the emitting region attenuates C IV and other resonance lines as expected, (6) there is evidence for depletion of Si and Fe relative to other elements, (7) ram pressure can be measured much more directly than in past studies, (8) nonthermal pressure (magnetic or cosmic-ray) apparently dominates in the recombination zone of this filament, and (9) full preionization can be present in gas entering even low-velocity radiative shocks. New techniques are introduced for determining the completeness of a shock and for determining the preshock density without recourse to the standard density diagnostic line ratios. The morphology of the region is consistent with an identification of the filament as one edge of a converging conical shock set up when the Cygnus Loop blast wave encountered a cloud with radially decreasing density, centered near Miller's position 2.

Note added in manuscript.—We have recently obtained further observations of the [S II] and [O II] doublet ratios with the double spectrograph on the 5.0 m telescope at Mt. Palomar. In the vicinity of the long-slit echelle position, we derive an electron density of 98 ± 13 cm^{-3} (2 σ error), which is 2.5 times the density assumed in § IV. This makes the thermal pressure in

the recombination zone comparable with the thermal pressure of the X-ray emitting gas, but still only one-seventh the shock ram pressure. Thus, the discussion of nonthermal pressure and pressure disequilibrium still applies, but the requirements are less extreme. For instance, if the recombination zone is magnetically supported, the preshock magnetic field is 15 μG. The new observations will be discussed in a separate paper.

We gratefully acknowledge the help of the *IUE* and Kitt Peak Observatory staffs in acquiring the observational data, of G. Nassiopoulos for reducing the *IUE* data, of F. Seward for providing the *Einstein* data, and of B. Woodgate for stimulating discussions. This work has been supported by NASA Grants NAS5-87 and NAG 528 to the Smithsonian Astrophysical Observatory, NASA Grant NAG 5-629 to the University of Wisconsin, NASA Contract NAS 5-25451 and NASA Grant NGL 05-002-134 to Caltech, and the Visiting Scientist Program of the Smithsonian Institution.

REFERENCES

Allen, C. W. 1973, *Astrophysical Quantities* (3d ed.; London: Athlone).
Benvenuti, P., Dopita, M., and D'Odorico, S. 1980, *Ap. J.*, **238**, 601.
Bertschinger, E. 1986, *Ap. J.*, **304**, 154.
Binnette, L., Dopita, M. A., and Tuohy, I. R. 1985, *Ap. J.*, **297**, 476.
Blair, W. P., Kirshner, R. P., and Chevalier, R. A. 1982, *Ap. J.*, **254**, 50.
Boggess, A., *et al.* 1978, *Nature*, **275**, 372.
Bohlin, R. C., Holm, A. V., Savage, B. D., Snijders, M. A. J., and Sparks, W. M. 1980, *Astr. Ap.*, **85**, 1.
Braun, R., and Strom, R. G. 1986, *Astr. Ap.*, **164**, 208.
Bychkov, K. V., and Pikel'ner, S. B. 1975, *Soviet Astr. Letters*, **1**, 14.
Cassatella, A., and Harris, A. W. 1983, *IUE NASA Newsletter*, No. 23, p. 21.
Charles, P. A., Kahn, S. M., and McKee, C. F. 1985, *Ap. J.*, **295**, 456.
Chevalier, R. A. 1983, *Ap. J.*, **272**, 765.
Chevalier, R. A., and Imamura, J. N. 1982, *Ap. J.*, **261**, 543.
Contini, M., and Shaviv, G. 1982, *Ap. Space Sci.*, **85**, 203.
Cox, D. P. 1972*a*, *Ap. J.*, **178**, 143.
———. 1972*b*, *Ap. J.*, **178**, 159.
Cox, D. P., Hester, J. J., and Raymond, J. C. 1987, *Ap. J.*, in preparation.
Cox, D. P., and Raymond, J. C. 1985, *Ap. J.*, **298**, 651.
DeNoyer, L. K. 1975, *Ap. J.*, **196**, 479.
Dopita, M. A. 1977, *Ap. J. Suppl.*, **33**, 437.
Dopita, M. A., Binnette, L., and Schwartz, R. D. 1982, *Ap. J.*, **261**, 183.
Eichler, D. A. 1985, *Ap. J.*, **294**, 40.
Falle, S. A. E. G. 1975, *M.N.R.A.S.*, **172**, 55.
Fesen, R. A., Blair, W. P., and Kirshner, R. P. 1982, *Ap. J.*, **262**, 171.
———. 1985, *Ap. J.*, **292**, 29.
Fesen, R. A., and Itoh, H. 1985, *Ap. J.*, **295**, 43.
Hartigan, P., Raymond, J. C., and Hartmann, L. 1987, *Ap. J.*, **316**, 323.
Heathcote, S. R., and Brand, P. W. J. L. 1983, *M.N.R.A.S.*, **203**, 67.
Hester, J. J. 1987, *Ap. J.*, **314**, 187.
Hester, J. J., and Cox, D. P. 1986, *Ap. J.*, **300**, 675.
Hester, J. J., Parker, R. A. R., and Dufour, R. J. 1983, *Ap. J.*, **273**, 219 (HPD).
Hester, J. J., Raymond, J. C., and Danielson, G. E. 1986, *Ap. J.* (*Letters*), **303**, L17.
Innes, D. E., Giddings, J. R., and Falle, S. A. E. G. 1986, in *Workshop on Model Nebulae*, ed. D. Pequinot (Paris: Observatoire de Paris), p. 153.
Kirshner, R. P., and Arnold, C. N. 1979, *Ap. J.*, **229**, 147.
Ku, W. H.-M., Kahn, S. M., Pisarski, R., and Long, K. S. 1984, *Ap. J.*, **278**, 615.
McCray, R., Stein, R. F., and Kafatos, M. 1975, *Ap. J.*, **196**, 565.
McKee, C. F., and Cowie, L. L. 1975, *Ap. J.*, **195**, 715.
McKee, C. F., Hollenbach, D. J., Seab, C. G., and Tielens, A. G. G. M. 1986, preprint.
Miller, J. S. 1974, *Ap. J.*, **189**, 239.
Minkowski, R. 1958, *Rev. Mod. Phys.*, **30**, 1048.
Nussbaumer, H., and Storey, P. J. 1986, preprint.
Panek, R. 1982, *IUE NASA Newsletter*, No. 18, p. 68.
Parker, R. A. R. 1967, *Ap. J.*, **149**, 363.
———. 1973, *Bull. AAS*, **5**, 393.
Pequinot, D. 1986, in *Workshop on Model Nebulae*, ed. D. Pequinot, (Paris: Observatoire de Paris), p. 363.
Poveda, A., and Woltjer, L. 1968, *A.J.*, **73**, 65.
Raymond, J. C. 1979, *Ap. J.*, **39**, 1.
Raymond, J. C., and Smith, B. W. 1977, *Ap. J. Suppl.*, **35**, 419.
Raymond, J. C., Black, J. H., Dupree, A. K., Hartmann, L., and Wolff, R. S. 1980, *Ap. J.*, **238**, 881.
———. 1981, *Ap. J.*, **246**, 100.
Raymond, J. C., Blair, W. P., Fesen, R. A., and Gull, T. R. 1983, *Ap. J.*, **275**, 636.
Schiffer, F. J. 1980, *IUE NASA Newsletter*, No. 9, p. 32.
Seab, C. G., and Shull, J. M. 1983, *Ap. J.*, **275**, 652.
Seaton, M. J. 1979, *M.N.R.A.S.*, **187**, 75p.
Shull, J. M., and McKee, C. F. 1979, *Ap. J.*, **227**, 131.
Shull, P. J., Jr., Parker, R. A. R., Gull, T. R., and Dufour, R. J. 1982, *Ap. J.*, **253**, 682.
Smith, M. D., and Dickel, J. R. 1983, *Ap. J.*, **265**, 272.
Straka, W. C. 1974, *Ap. J.*, **190**, 59.
Straka, W. C., Dickel, J. R., Blair, W. P., and Fesen, R. P. 1986, *Ap. J.*, **306**, 266.

WILLIAM P. BLAIR: Department of Physics and Astronomy, Johns Hopkins University, 170 Rowland Hall, Baltimore, MD 21218

DON P. COX: Department of Physics, 1150 University Avenue, University of Wisconsin, Madison, WI 53706

ROBERT A. FESEN: CASA, University of Colorado, Campus Box 391, Boulder, CO 80309

THEODORE R. GULL: Code 680, NASA/GSFC, Greenbelt, MD 20771

J. JEFF HESTER: Division Geological and Planetary Science, 170–25, California Institute of Technology, Pasadena, CA 91125

JOHN C. RAYMOND: Center for Astrophysics, 60 Garden Street, Cambridge, MA 02138